



# Multi-annual and multi-decadal evolution of sediment accretion in a saltmarsh of the French Atlantic coast: Implications for carbon sequestration

B. Amann, E. Chaumillon, S. Schmidt, L. Olivier, J. Jupin, M.C. Perello, J.P. Walsh

## ► To cite this version:

B. Amann, E. Chaumillon, S. Schmidt, L. Olivier, J. Jupin, et al.. Multi-annual and multi-decadal evolution of sediment accretion in a saltmarsh of the French Atlantic coast: Implications for carbon sequestration. *Estuarine, Coastal and Shelf Science*, 2023, 293, pp.108467. 10.1016/j.ecss.2023.108467 . hal-04276241

**HAL Id: hal-04276241**

**<https://hal.science/hal-04276241>**

Submitted on 8 Dec 2023

**HAL** is a multi-disciplinary open access archive for the deposit and dissemination of scientific research documents, whether they are published or not. The documents may come from teaching and research institutions in France or abroad, or from public or private research centers.

L'archive ouverte pluridisciplinaire **HAL**, est destinée au dépôt et à la diffusion de documents scientifiques de niveau recherche, publiés ou non, émanant des établissements d'enseignement et de recherche français ou étrangers, des laboratoires publics ou privés.

**Multi-annual and multi-decadal evolution of sediment accretion in a saltmarsh of the French Atlantic coast: implications for carbon sequestration**

Amann, B.<sup>1</sup>, Chaumillon, E.<sup>1</sup>, Schmidt, S.<sup>2</sup>, Olivier, L.<sup>1</sup>, Jupin, J.<sup>3</sup>, Perello, M. C.<sup>2</sup>, Walsh, J. P.<sup>4</sup>

<sup>1</sup> Littoral ENvironnement et Sociétés (LIENSs) - UMR 7266 CNRS, La Rochelle Université, 17000 La Rochelle, France

<sup>2</sup> Univ. Bordeaux, CNRS, Bordeaux INP, EPOC, UMR 5805, F-33600 Pessac, France

<sup>3</sup> Posgrado en Ciencias del Mar y Limnología, Universidad Nacional Autónoma de México. Av. Universidad 3000, Ciudad 6 Universitaria, Coyoacán, 04510 Ciudad de México, Mexico

<sup>4</sup> Coastal Resources Center, University of Rhode Island, Kingston, RI 02881, USA

**Highlights**

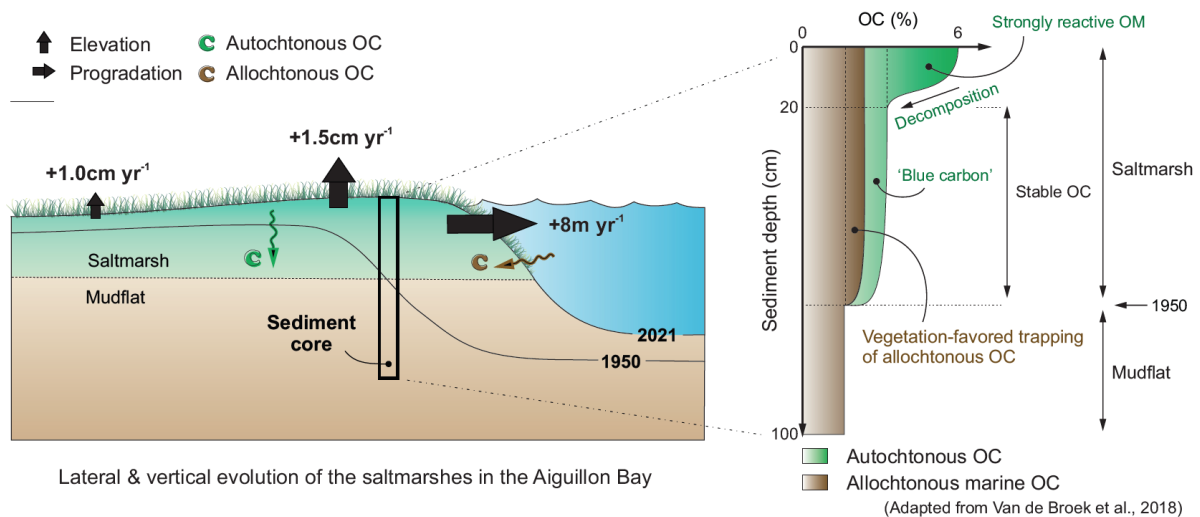
- Saltmarshes prograde and aggrade at very high rates, keeping up with sea level rise
- Sediment source proximity and accommodation space explain SAR spatial variability
- Organic carbon accumulation rates are highly variable at the scale of a bay
- Allochthonous C of marine origin prevails in long-term C sequestration

**Key words:** <sup>210</sup>Pb – LiDAR – organic carbon origin – Minerogenic saltmarsh – Blue Carbon – Nature-based solutions

## Abstract

Coastal marshes offer natural solutions for adapting to and mitigating the effects of climate change and sea level rise. However, the resilience of the marsh physical system and, with it, the ecosystem services that it provides, is largely site specific. This calls for the increase in the spatial cover of coastal marsh studies in order to assess the controlling factors of marsh evolution, and their long-term carbon storage capacities. Here, we study the spatio-temporal variations in sedimentation rates and organic carbon (OC) sequestration capacity of the macrotidal minerogenic saltmarshes in Aiguillon Bay, belonging to one of the largest French coastal marshes. Supported by aerial photographs and satellite image analysis, we first show that saltmarshes of the Aiguillon Bay have prograded at very high rates, up to  $14 \text{ m yr}^{-1}$  since 1950. Sediment accumulation rates (SAR) were estimated at both multi-annual to multi-decadal scales based on two approaches: (i) LiDAR-based digital elevation models from multiple acquisition dates (2010-2021); and (ii) depth profiles of  $^{210}\text{Pb}$  in excess and  $^{137}\text{Cs}$  in sediment cores collected along cross-shore transects in the saltmarshes. Long-term SAR range from  $0.8$  to  $2.2 \text{ cm yr}^{-1}$  and are among the highest reported worldwide for equivalent systems. The positive accretion balance (accretion rate minus local sea-level rise rate) provides important clues on marsh resilience suggesting that the Aiguillon Bay is currently able to adapt to rising sea level. Despite relatively low organic carbon content ( $1.3$  to  $6.0 \%$ ), high SAR leads to high carbon sequestration rates ( $99$ - $345 \text{ gC m}^{-2} \text{ yr}^{-1}$ ; or a mean value of  $2.5 \text{ Mg C ha}^{-1} \text{ yr}^{-1}$ ). The isotopic signature of sediment OC reveals a significant and rapid decomposition of organic material in surface cores, while allochthonous sediment of marine origin dominates the signature of chemically-stable OC of marsh sediments. This implies that the carbon sequestration capacity of minerogenic saltmarshes, such as those of the Pertuis Charentais, also depends upon the wealth of adjacent coastal environments through high sediment supply and primary productivity.

## Graphical Abstract



## 1. Introduction

Saltmarshes offer natural solutions for adapting to and for mitigating the effects of global changes (Bertram et al., 2021; Costanza et al., 2014). Beyond many services such as ecological nurseries, tidal saltmarshes constitute a natural barrier against marine submersion, through their ability to accumulate sediment and to rise at the same time as the sea level, especially in macrotidal coastal areas (Crosby et al., 2016; Fagherazzi et al., 2020; Rogers et al., 2019). They protect the hinterland from flooding through their capacity to attenuate storm surges and waves, and they also offer natural solutions to buffer nutrient and pollutant inputs and to challenge the loss of biodiversity (Bij de Vaate et al., 2020; Leonardi et al., 2018). Saltmarshes are also critical environments for sediment organic carbon (OC) accumulation. Included in the 'blue carbon ecosystems' with mangroves and seagrass beds, saltmarshes contribute actively to the global carbon sink with burial rates of up to 15 Tg C yr<sup>-1</sup> (Lovelock and Reef, 2020; Macreadie et al., 2019). The blue-carbon function is increasingly recognized as an important lever for climate change mitigation, and for the implementation of nature-based solutions in particular (Hendriks et al., 2020; IPCC, 2022; Vinent et al., 2019).

The geomorphological evolution of saltmarshes largely controls the conservation of the ecosystem services they provide. The resilience of the marsh physical system and its biota is largely site specific and depends upon various conditions such as the tidal regime, the sediment supply, and the exposure to wind and waves (Fagherazzi et al., 2020). Saltmarshes are dynamic systems able to develop laterally, and to elevate their topography in response to sea level rise. Thus, fully understanding its horizontal and vertical dynamics is key to determining their fate in the next decades. This is particularly relevant for the OC sequestration potential (Lovelock and Reef, 2020).

Despite considerable scientific efforts, the number of saltmarsh studies remain under-represented compared to studies on mangroves and seagrass (e.g., 13% of valuation studies for blue carbon ecosystems concern saltmarshes, for the period 2007-2018; Himes-Cornell et al., 2018), and they do not yet warrant accurate upscaling of carbon sequestration rates at a continental or global scale (Macreadie et al., 2019). As an example, a single French study (Hensel et al., 1999) is considered in the first blue carbon review by Chmura et al., (2003), and resumed in subsequent ones (e.g., Duarte et al., 2005; Mcleod et al., 2011; Ouyang and Lee, 2014; Regnier et al., 2022). This calls for the increase in the spatial cover of coastal studies in order to evaluate the role of forcing parameters on marsh evolution, and on their long-term carbon sequestration and storage capacities (Ouyang and Lee, 2022). Also, while carbon stocks (e.g., in Mg C ha<sup>-1</sup>) are generally well identified, carbon accumulation rates from coastal habitats are rarely addressed (in Mg C ha<sup>-1</sup> yr<sup>-1</sup>; Arias-Ortiz et al., 2018; Jennerjahn, 2020). Recent reviews on blue carbon research also stressed the need to improve our understanding of the source and stability of OC in saltmarshes (Macreadie et al., 2019; Windham-Myers et al., 2019).

In this context, the French Atlantic coast offers a good opportunity to contribute to the global catalogue of saltmarsh studies by documenting sediment and carbon accumulation rates from macrotidal systems. Here we study saltmarshes of the Aiguillon Bay; a highly dynamic system that is connected to small rivers. Seaward shoreline migration was shown at both long- and medium-time scales, respectively with rates of 70 km over the last 2000 years (Chaumillon et al., 2004) and up to 7 ha an<sup>-1</sup> during the last 50 years (Godet et al., 2015). This suggests that the Aiguillon Bay potentially accumulates a large amount of sediment and maintains an efficient carbon sequestration capacity.

With this in mind, our study aims at: (i) understanding the morphological evolution of saltmarshes; and (ii) quantifying the long-term carbon sequestration capacity of these coastal wetlands. First, we build up a picture of the lateral and vertical evolution of the Aiguillon marshes at the multi-annual and multi-decadal time scales. For this, we combine the reconstruction of the saltmarsh boundary through aerial and satellite imagery analysis, with sediment accumulation rates derived by two methods: (i) <sup>210</sup>Pb-

derived dating of sediment cores collected along two cross-shore transects; and supported by (ii) LiDAR-based digital elevation models from multiple acquisition dates. Then, we discuss the origin and fate of organic material (OM) preserved in coastal environments using elemental OC content, C/N,  $\delta^{13}\text{C}$ , and  $\delta^{15}\text{N}$  from landward and seaward locations. Finally, we discuss the rapid accumulation of sediment and the relatively high carbon sequestration capacity of the studied saltmarshes, with respect to the international literature. Our results may provide a decision support tool for the implementation of nature-based solutions in coastal management strategies (e.g., Dupuy et al., 2022).

## 2. Study site

The Aiguillon Bay is located on the southwestern Atlantic French coast, which opens onto the Pertuis Breton between Ré Island and the Vendée Coast (Fig. 1). The Pertuis Breton forms a major embayment opened to the Atlantic Ocean that corresponds to the drowned incised valley segment of the Lay, Sèvre Niortaise, and Vendée Rivers (Chaumillon et al., 2008).

The Aiguillon Bay is a cove, semi-enclosed by the so-called “Pointe de l'Aiguillon”, a sand spit developing from the northwest to the southeast (Fig. 1). It is characterized by lowland coastal environments, which include one of the largest coastal marshes of France (1100 ha) fronted by extensive tidal flats (3700 ha). The cove receives freshwater and a part of the fine sediments from the Sèvre Niortaise ( $12 \text{ m}^3 \text{ s}^{-1}$ ) and the Lay rivers ( $2 \text{ m}^3 \text{ s}^{-1}$ ) predominantly (Banque HYDRO, 1969/2017), and from several smaller channels secondarily (Coignot et al., 2020; Fig. 1). This region of the French coast is characterized by relatively high suspended sediment concentrations with  $4.0 \pm 3.1 \text{ mg L}^{-1}$  reported locally (SOMLIT station, Pertuis Antioche; period 04.2020 – 03.2022; [www.somlit.fr](http://www.somlit.fr)). However, the fine sediment supply to the Aiguillon Bay is not well understood. Erosion of coastal Mesozoic limestones and marls outcrops may provide significant quantities of clay particles to the bay. It cannot be excluded that fine sediments are also supplied by the Gironde Estuary, whose sediment input to coastal waters was estimated to  $1.6 \text{ Mt yr}^{-1}$  (Doxaran et al., 2009; Schmitt and Chaumillon, 2023). The dispersion of the estuarine plume of the Gironde could reach the Marennes-Oléron Bay located 45 km in the south of the Aiguillon Bay (Constantin et al., 2018; Poirier et al., 2016).

The area is characterized by a semi-diurnal macrotidal regime with mean tidal range of c. 4 meters and strong tidal currents (Dodet et al., 2019). This part of the French coastline is characterized by low-lying coastal zones particularly vulnerable to flooding (Baumann et al., 2017; Bertin et al., 2014; Breilh et al., 2014, 2013). The studied area has experienced six major marine floods over the 20<sup>th</sup> and 21<sup>st</sup> centuries (Breilh et al., 2014). The last major marine flood was caused by the storm Xynthia (28/02/2010), which induced an exceptional storm surge (1.6 m in La Rochelle Harbor) in phase with high spring tide resulting in extensive flooding of low-lying coastal zones (Bertin et al., 2012; Breilh et al., 2013).

The Aiguillon Bay bears witness to the successive land reclamation history of the Marais Poitevin, which have gradually reduced the ancient Gulf of Pictons (Godet et al., 2015; Godet and Thomas, 2013; Verger, 2009; Fig. 1a). Today, the bay includes 1100 ha of saltmarshes among which about half is subject to mowing (Fig. 1c, d). The halophytic vegetation is dominated by C3 plants such as marine *Puccinellia* (*puccinellia maritima*) and Sea Purslane (*halimione portulacoides*). C4 plants are also present, with *Agropyron* (*agropyron pungentis*) that commonly develop in topographic high, while Marine *Spartina* (*Spartina maritima*) and a few annual *Salicornia* (*Salicornia sp*) compose lowland areas of the saltmarsh (Fig. S1). The Aiguillon Bay has been fully classified as a National Nature Reserve in 1999 for its fauna and ornithological richness.

### 3. Materials and methods

#### 3.1. Aerial & satellite imagery

Aerial photographs and satellite images were used to reconstruct the lateral evolution of the saltmarsh boundary (boundary between the mudflat and the saltmarsh) in the Aiguillon Bay, from 1950 to 2020. Digitized aerial photographs from 1950 to 2010 (source: *IGN, France*) were mosaicked, georeferenced and ortho-rectified using Geomatica v.9® software. The mapping of the bay did not integrate marshes located in the meander of the Sèvre Niortaise. Roads and parking areas around the bay were used as control points for the geo-referencing. The most recent evolutions of the saltmarshes were derived using the SPOT-6 Satellite Image Gallery, for the years 2015-2020. The spatial uncertainty (SU) was estimated following (Ford, 2012):

$$SU = \sqrt{PU^2 + GU^2 + DU^2} \quad (\text{in m})$$

where PU, GU and DU are the pixel size, Geo-referencing, and Digitizing Uncertainties, respectively. PU and GU were derived from the metadata of the source images (Table S1), while DU was estimated from digitizing replicates of aerial photographs and orthophotos.

The rate of progression of the saltmarsh boundary (in m yr<sup>-1</sup>) was calculated for the period 1950-2020 using the USGS DSAS v5 tool (Himmelstoss et al., 2018). For this, a baseline was generated from a buffer zone of 100 m around the combined vegetation lines of 1950, and the seaward part of the buffer zone was defined using the tracing tool from the 2020 imagery. Cross-shore transects were defined in this way, every 50 m covering the entire bay. A mean SU of 8.8 m was implemented into the DSAS v5 calculations, for the period 1950-2020. A tolerance of 20 m and a smoothing of 1000 were assigned.

#### 3.2. Sediment coring and processing

##### 3.2.1. Sediment coring

Five sediment cores were collected from two cross-shore transects of the Aiguillon Bay saltmarshes, using a Russian corer; one core was collected in July 2017, and four in June 2021 (Fig. 1). The coring sites were selected to meet the following criteria: (i) they are placed on the saltmarsh boundary mapped for a given year, thus allowing to constrain the age of the transition between a pre-existing mudflat environment and the saltmarsh; (ii) they are representative of the ecosystem of the bay covering landward, seaward and intermediate zones of the saltmarsh; and (iii) the targeted marsh soil profiles develop under the same management type over the decades, namely free of mowing activity, thus focusing on the 'natural' evolution of the saltmarshes of the bay. Three 1.1-m long cores were thus collected along a cross-shore transect from the northern bay (AIG21\_20, AIG21\_21, and AIG21\_22; Fig. 1b). AIG21\_22 was retrieved from the high marsh dominated by a C4-plant environment (Marine *Puccinellia*, and Sea Purslane), hereafter mentioned as the landward site. AIG21\_20 was retrieved from the low marsh close to the ocean characterized by the presence of C3 and C4 plants (e.g., Marine *Spartina*), hereafter mentioned as the seaward site. AIG21\_21 corresponds to the intermediate location. Two short cores (length < 50 cm) were collected from saltmarshes located at the mouth of the Sèvre Niortaise River in order to assess the influence of river proximity on sedimentation rates and carbon accumulation potential (AIG21\_11, AIG17\_01; Fig. 1c; Fig. S2).

### 3.2.2. Dry bulk density

Each 2021 core was sectioned at a 1cm resolution, and samples were freeze-dried for 72 h to determine the water content, the dry bulk density (DBD), and radionuclides of interest. The 2017 core was only sampled every 4 cm. All samples were ground gently using a mortar for further analyses.

### 3.2.3. Organic matter content, TOC, TN, $\delta^{13}\text{C}$ and $\delta^{15}\text{N}$

High-resolution (every 1 cm) and cost-effective profiles of organic matter (OM) content were first obtained using loss on ignition (LOI) to constrain the sample selection for elemental and isotope analyses of carbon and nitrogen. The LOI analysis was performed at a temperature of combustion of 550°C for 14 h (Baustian et al., 2017; Wilson and Allison, 2008). Due to the diversity of temperatures and durations used for LOI in the literature, the protocol with the lowest reported temperature of combustion (450°C for 8 h) was also tested for comparison (Craft et al., 1991; Howard et al., 2014; Fig S3). We used an elemental analyzer (EA Isolink, Thermo Scientific) to measure organic carbon and total nitrogen contents from selected samples in each core.

Total organic carbon (TOC), total nitrogen (TN), and  $\delta^{13}\text{C}$  and  $\delta^{15}\text{N}$  isotopes were determined on the 2021 sediments using an EA-IRMS at the LIENSs Stable Isotope Facility, La Rochelle University, France (EA Isolink, Thermo Scientific; Delta V Plus with a Conflo IV interface, Thermo Scientific). The analyses were duplicated on samples after acidification for TOC and  $\delta^{13}\text{C}$ , and on raw samples for  $\delta^{15}\text{N}$  to prevent the effects of acidification on  $\delta^{15}\text{N}$  values (Lebreton et al., 2011). A correction factor was applied to the TOC measurements using total nitrogen as a proxy for the changing weight induced by sample acidification. 100 mg of dry sediment were acidified with 0.5N HCl to remove the carbonates, and dried overnight in a dry bath at 60°C under N<sub>2</sub> filtered airflow. 1 mL MilliQ water was then added to the sample, which was freeze-dried and grounded again. An optimal weight of 5 mg of sediment was added to 8 x 5 mm tin capsules for analysis. Isotopic values were expressed in the  $\delta$  unit notation as deviations from standards (Vienna Pee Dee Belemnite for  $\delta^{13}\text{C}$  and atmospheric N<sub>2</sub> for  $\delta^{15}\text{N}$ ) following the formula:

$$\delta^{13}\text{C} \text{ or } \delta^{15}\text{N} = \left( \frac{R_{\text{sample}}}{R_{\text{standard}}} - 1 \right) \cdot 10^3, \text{ where } R \text{ is } ^{13}\text{C}/^{12}\text{C} \text{ or } ^{15}\text{N}/^{14}\text{N}, \text{ respectively}$$

Reference materials USGS-61 and USGS-63 (Caffeine) were used for calibration and for uncertainty calculation. Standard deviations were 0.11 % for carbon, 0.10 % for nitrogen, and 0.05 ‰ for  $\delta^{13}\text{C}$  and 0.04 ‰ for  $\delta^{15}\text{N}$ .

The TOC content measured by elemental analysis was used to calculate organic carbon accumulation rates in each sediment core. Sediment  $\delta^{13}\text{C}$  and  $\delta^{15}\text{N}$  combined with C/N ratios were used to assess the origin of OC; namely to distinguish between an autochthonous and an allochthonous source. Below-ground biomass (BGB) was separated from the bulk sediment in top cores and also analyzed by EA-IRMS following the same protocol as for the bulk sediment.

### 3.2.4. Sediment grain size

Grain-size analysis was performed every three samples using a Malvern Mastersizer 2000 laser particle size analyzer at EPOC (France). Sample selection followed those of the sampling strategy for dating in order to assess a potential effect of changing grain size on the age-depth modeling. Prior to analysis, the terrigenous fraction was isolated by removing organic matter, calcium carbonate, and biogenic silica through H<sub>2</sub>O<sub>2</sub> (35%), HCl (10 to 50%), and NaOH (1N) chemical pre-treatments, respectively. Due to the high organic matter content, this pre-treatment and grain size analysis were performed after combustion of the sediment samples for 14h at 550°C. Adjustment of the material optical properties was needed in order to reduce the weighted residuals induced by the red color of these pre-combusted materials. For this, the refractive and absorption index of red pigments were selected from the optical

property analyzer tool of the Malvern 2000 software (RI = 2.52, AI = 0.1, respectively). This ensured an optimal fit between measured and modeled grain size data. Finally, a solution of sodium hexametaphosphate (NaPO<sub>3</sub>, 2%) was used to prevent clay flocculation before analysis. Grain-size distribution averages were obtained from three replicates, each measured for 12 s after 10% sonication.

### 3.2.5. Sediment, mass and organic carbon accumulation rates

Sediment accumulation rates (SAR, in cm yr<sup>-1</sup>) and mass accumulation rates (MAR, in g cm<sup>-2</sup> yr<sup>-1</sup>) at the multi-decadal scale were obtained using <sup>210</sup>Pb-based dating of the cores. <sup>210</sup>Pb (T<sub>1/2</sub> = 22.3 years) is a naturally-occurring radionuclide delivered continuously on Earth surface by atmospheric fallout and readily scavenged by particulate matter. This atmospherically derived <sup>210</sup>Pb is referred to as <sup>210</sup>Pb in excess (<sup>210</sup>Pb<sub>xs</sub>) of that supported in sediment derived from the *in situ* radioactive decay series of <sup>238</sup>U (Iurian et al., 2021, and references herein). The <sup>210</sup>Pb-based SAR were independently checked by the artificial radionuclide <sup>137</sup>Cs (T<sub>1/2</sub> = 30 years), which presents a maximum atmospheric fallout related to weapon tests in 1963.

For the cores collected in 2021, the activities of the radioelements of interest (<sup>210</sup>Pb, <sup>226</sup>Ra, <sup>232</sup>Th, <sup>137</sup>Cs) were measured using a high-efficiency, low-background broad energy gamma detector equipped with a Cryo-Cycle II (Mirion) at EPOC, University of Bordeaux (Dubosq et al., 2021). <sup>226</sup>Ra was determined using selected gamma rays emitted by its short-lived decay products (<sup>214</sup>Pb and <sup>214</sup>Bi), implying that measurements were performed at least 3 weeks after 6-8 g aliquots of dry sediment were placed in the counting vials to ensure equilibrium. <sup>210</sup>Pb, <sup>232</sup>Th and <sup>137</sup>Cs were determined by their gamma ray at 46.5, 238 and 662 keV, respectively (Reyss et al, 1995). Calibration of the detector was obtained using certified reference material (IAEA-RGU-1; SOIL-6). For AIG17\_01, <sup>210</sup>Pb was measured by alpha spectrometry following the methodology described in Corbett and Walsh (2015). Activities are expressed in mBq g<sup>-1</sup> and errors calculated using 1-standard deviation counting statistics. Excess <sup>210</sup>Pb was calculated by subtracting the measured <sup>226</sup>Ra from the total measured <sup>210</sup>Pb activity. <sup>210</sup>Pb was normalized considering <sup>232</sup>Th in order to reduce the impact of changes in sediment composition (Stupar et al., 2014), due to a variable proportion of vegetal fraction in saltmarsh sediments. Sediment and mass accumulation rates were determined from the slope of the <sup>210</sup>Pb<sub>xs</sub><sup>Th</sup> profiles against depth and cumulative mass, using the CF:CS model (constant flux and constant sedimentation). For AIG17-01, calculations were done on <sup>210</sup>Pb<sub>xs</sub> in the absence of <sup>232</sup>Th determination. The mudflat/marsh transition in the core was determined by matching information based on: (i) marsh vegetation boundaries mapped at different years from aerial photos and satellite images, (ii) <sup>210</sup>Pb dating of the sediments downcore, and (iii) changes in the isotopic signature of the sedimentary organic matter.

Organic carbon accumulation rates (CAR, in g cm<sup>-2</sup> yr<sup>-1</sup>) were calculated as the product of the mean sediment OC content (in %), and mass accumulation rates based on the <sup>210</sup>Pb<sub>xs</sub><sup>Th</sup> profiles of the sediment cores (in g cm<sup>-2</sup> yr<sup>-1</sup>). The sections of the OC and δ<sup>13</sup>C profiles reaching a rather constant and minimum value in depth (< 2\*standard deviation) were interpreted as the effectively-preserved OC stocks, thus representing the long-term carbon sequestration capacity of the saltmarsh. In topsoil sediments, labile autochthonous OC inputs can control short-term OC deposition rates (Mueller et al., 2019; Van de Broek et al., 2018). Thus, the upper section of each core was excluded from the CAR calculation to avoid an overestimation of the long-term OC sequestration rates (expressed in Mg C ha<sup>-1</sup> yr<sup>-1</sup>).

### 3.3. LiDAR data



Saltmarsh accumulation rates at the multi-annual scale were obtained from LiDAR-derived digital elevation models (DEMs) obtained from 2010 to 2021. SAR estimates from LiDAR data are used to support the orders of magnitude in SAR obtained at the multi-decadal scale by sediment core analysis. LiDAR is a generalized remote-sensing method used to gauge the evolutions at the earth's surface. By measuring the reflected light that bounces off the ground and back to the sensor fixed on a plane, it provides accurate mapping of surface elevation from coastal environments (Collin et al., 2010; Medeiros et al., 2022). Differences between DEMs obtained during successive years were used to map surface elevation changes and to assess short-term sediment accumulation rates in the Aiguillon saltmarshes.

The most recent LiDAR data were acquired for the entire bay in September 2016 and October 2021 (*OPSIA Company, Toulon*). Data were collected using a laser scanner RIEGL VQ-780 II mounted on a Partenavia P68 Observer2 from an altitude of 750 m and 1650 m in 2016 and 2021, respectively. It provided a gaining density of 10 points/m<sup>2</sup>. The vertical accuracy was derived from twenty ground-control points (GCPs) using a RTK-GPS on roads and parking around the bay. The root mean squared error for the height difference between LiDAR and RTK-GPS data was 2.5 and 3.4 cm for 2016 and 2021, respectively (Table S1). Previous LiDAR data were collected in July 2010, and in February 2013. These data were acquired with a point density of 3 points/m<sup>2</sup> using a laser scanner RIEGL VQ-820-G in 2010 (*Institut Géographique National IGN, France*), and using a laser scanner RIEGL LiteMapper-6800 in 2013 (*Aerodata Company, Marcq-en-Baroeul, France*). 376 GCPs were defined, and the vertical accuracy was calculated by comparing LiDAR data of 2010 and 2013, with the reference LiDAR data of 2016. This resulted in a vertical accuracy of 7 and 2 cm for 2010 and 2013, respectively (Table S2).

Differences in LiDAR-based DEMs were used to assess short-term (decadal) sediment accumulation rates by estimating the volume of sediment accumulated over saltmarshes of the whole bay, through time (in m<sup>3</sup>). These estimates accounted for marsh-elevation changes and for the progradation of the saltmarsh boundary between two periods of acquisition. The sediment volume in the salt marsh was then divided by the salt-marsh area to calculate mean sediment accumulation rates over different periods (2010-2021, 2013-2021, and 2016-2021; Table 2). Sediment accumulation rates for the entire instrumental period 2010 to 2021 were used to support orders of magnitude in accumulation rates derived from <sup>210</sup>Pb-derived dating of sediment cores. This integration of LiDAR data over 11 years has the advantage of reducing uncertainties associated with the vertical accuracy of each annual DEM. Contrary to sediment core data, LiDAR data covers the entire bay that allows us discussing the spatial and temporal variability of saltmarsh accretion over the last 20 years. Because TOC measurements are bound to the multi-decadal time scale, LiDAR data was not used to calculate carbon accumulation rates at the multi-annual time scale.

## 4. Results

### 4.1. Lateral evolution of the saltmarshes

The reconstruction of the saltmarsh boundary using aerial photographs and satellite images shows a global progradation toward the ocean since 1950 (Fig. 2). Data disclose a mean gradual seaward migration of  $8 \text{ m yr}^{-1}$  for the whole bay, and a maximum of  $14 \text{ m yr}^{-1}$  for the northern bay (Fig. 2a). This corresponds to a mean net gain in saltmarsh area of  $8 \text{ ha yr}^{-1}$  (Fig. 2b). The most recent land reclamations date back to 1963 and 1965, and are located in the southeastern and the northwestern bay, respectively. These land claims induced a reduction of 200 ha in the saltmarsh area, from 1960 to 1972 (Fig. 2b). The saltmarsh has gained surface at relatively constant pace throughout the last two decades. The greatest progradation is in the northern bay, close to the Chenal Vieux and between vegetated tips that develop all around the bay (Fig. 2a).

### 4.2. Sediment composition

Sediments of the Aiguillon bay are composed predominantly of fine silt and clay at  $81 \pm 5 \%$  and  $17 \pm 5 \%$  respectively, with mean grain size of  $6.7 \pm 1.6 \mu\text{m}$  (Fig. 3). OM content ranges from 12 to 24 %, and OC content from 1.1 to 6.1 % (Fig. S3), with the highest values found in the top of the sediment cores. These rather low OC levels categorize the saltmarshes of the Aiguillon Bay as minerogenic marshes; i.e., marshes that are dominated by mineral sediment input supplied by the inundating water.

Along the northern transect, AIG21\_22 core presents a clear change at 20 cm depth. OM and OC content are maximal at the surface of the core until 7.5 cm, with a mean OC value of 4.5 % (Fig. 3). This value quickly drops to 2.7 % until 20 cm, and then reaches a minimum and relatively stable value of  $1.4 \pm 0.1 \%$  until the base of the core. Maximum OC values are also found at the surface of the cores of AIG21\_21 and AIG21\_20 with 3.7 % and 3.5 %, respectively. These values decrease significantly with depth and stabilize below 20 cm in both cores, with mean OC of  $1.7 \pm 0.2 \%$  and  $2.3 \pm 0.2 \%$  for AIG21\_20 and AIG21\_21, respectively.

The three cores contrast by their carbon and nitrogen isotopic profiles.  $\delta^{13}\text{C}$  is minimal at the surface of cores AIG21\_22 and AIG21\_21 with mean values of  $-26.4 \text{ ‰}$  and  $-23.6 \text{ ‰}$ , respectively. This value increases downcore reaching a mean of  $-22.0 \text{ ‰}$  for AIG21\_22 and  $-18.1 \text{ ‰}$  in AIG21\_21, towards the base of the cores. The  $\delta^{13}\text{C}$  profile of the seaward site AIG21\_20 presents an opposite pattern with maxima found at the surface averaging  $-16.9 \text{ ‰}$ , and a mean of  $-21.9 \text{ ‰}$  found towards the base.  $\delta^{15}\text{N}$  gradually decreases with depth in all cores. This trend is more pronounced in AIG21\_22 with a surface value of  $9.4 \text{ ‰}$  and a minimum of  $6.9 \text{ ‰}$  found at the base of the core. AIG21\_21 shows a decrease from  $8.7 \text{ ‰}$  to  $7.0 \text{ ‰}$ , and AIG21\_20 from  $7.7 \text{ ‰}$  to  $7.3 \text{ ‰}$ .

Along the eastern transect, the short core AIG21\_11 show profiles of OC and  $\delta^{13}\text{C}$  similar to that of the landward site AIG21\_22 (Fig. S2). OC content decreases from 6.1 % at the surface to 1.5 % at the core basal.  $\delta^{13}\text{C}$  is enriched from surface to base, with mean values ranging from  $-26.6 \text{ ‰}$  to  $-19.6 \text{ ‰}$ .

Grain size does not differ significantly between cores and between samples within each core, with geometric mean grain size of  $7.6 \mu\text{m}$  for AIG21\_22,  $6.4 \mu\text{m}$  for AIG21\_21, and  $6.2 \mu\text{m}$  for AIG21\_20. This suggests that bulk sediment material accumulated in saltmarshes of the Aiguillon Bay is unchanged through time and between locations.

### 4.3. Vertical evolution of the saltmarshes

#### 4.3.1. Sediment and mass accumulation rates

$^{210}\text{Pb}_{\text{xs}}$  activities are quite similar in surface sediment of all the cores (c. 100 mBq g<sup>-1</sup>), and decrease exponentially with sediment depth (Fig. 4). In contrast, the maximum penetration depth of  $^{210}\text{Pb}_{\text{xs}}$  is extremely variable among the cores. While negligible excesses are reached at about 80 cm in core AIG21\_22,  $^{210}\text{Pb}_{\text{xs}}$  activities are only half the surface values at 100 cm in core AIG21\_20. Even if such penetrations correspond to significant sedimentary accumulation, this suggests large disparities in the rate of sedimentation between the different sites. The decrease in  $^{210}\text{Pb}_{\text{xs}}$  present some irregularities as observed from 40 to 43 cm on core AIG21\_22 with lower excesses compared to the surrounding layers. Assuming that this layer corresponds to a specific event (relocation of older sediment), the evidence of this event was actively suppressed from the profile to produce an event-free  $^{210}\text{Pb}_{\text{xs}}^{\text{Th}}$  profile on which a mean SAR was calculated. This allows comparing long-term SAR estimates between the different cores in the Aiguillon saltmarshes.  $^{232}\text{Th}$  activities range between 28 to 55 mBq g<sup>-1</sup>, with the lowest values measured in the upper sections. Surface sediments also present the highest total carbon content resulting in a dilution of the detrital fraction as traced by the long-lived  $^{232}\text{Th}$  ( $T_{1/2} = 14 \cdot 10^9$  years). This dilution effect also has an impact on  $^{210}\text{Pb}$  as shown by the comparison of surface  $^{210}\text{Pb}_{\text{xs}}$  and  $^{210}\text{Pb}_{\text{xs}}^{\text{Th}}$  activities (Fig. 4). Th-corrected  $^{210}\text{Pb}_{\text{xs}}$  is thus preferred to avoid overestimating sediment accumulation rates.

The depth of the  $^{137}\text{Cs}$  peak corresponding to the year 1963 was also used to test the robustness of the sediment and mass accumulation rates derived from the  $^{210}\text{Pb}_{\text{xs}}^{\text{Th}}$  profiles.  $^{137}\text{Cs}$  activities are low (< 10 mBq g<sup>-1</sup>) in all profiles, except for a peak in core AIG-21\_22 and to a lesser extent in core AIG21\_21. In AIG21\_22, a clear  $^{137}\text{Cs}$  peak is found at 51 cm that lies within the error range of the  $^{210}\text{Pb}$  model that estimates a depth of  $49 \pm 3$  cm for this chronomarker. Similarly in AIG21\_21,  $^{137}\text{Cs}$  activity peaks at 106.5 cm, expected at  $107 \pm 5$  cm using the  $^{210}\text{Pb}$  model. The high sedimentation rates of AIG21\_20, as derived from the  $^{210}\text{Pb}$  model ( $2.2 \pm 0.3$  cm yr<sup>-1</sup>), does not allow pointing at the year 1963 for the 110-cm long sequence (projected depth of  $129 \pm 19$  cm). The  $^{137}\text{Cs}$  profile of AIG21\_20 thus shows a gradual increase with depth.

$^{210}\text{Pb}_{\text{xs}}^{\text{Th}}$  profiles result in high mean apparent sedimentation accumulation rates (SAR) ranging from 0.84 to 2.22 cm yr<sup>-1</sup>, with corresponding mass accumulation rates (MAR) of 0.74 to 1.83 g cm<sup>-2</sup> yr<sup>-1</sup> (Table 1). On the northern transect, the lowest sedimentation rates are found for the landward site (AIG21\_22), while the highest values are found for the seaward site (AIG21\_20). Short cores located close to the river mouth (AIG21\_11, and AIG17\_01) have intermediate values of 1.24 cm yr<sup>-1</sup> and 1.41 cm yr<sup>-1</sup> (0.86 and 1.24 g cm<sup>-2</sup> yr<sup>-1</sup>), respectively.

#### 4.3.2. Spatial and temporal variability of saltmarsh accretion using LiDAR data

LiDAR data demonstrate that the saltmarshes of the Aiguillon Bay have rapidly accumulated sediment over the last decade. A net sediment gain of  $1\,419\,043 \pm 458\,732$  m<sup>3</sup> was found between 2010 and 2021, which corresponds to a mean sedimentation rate of  $1.17 \pm 0.38$  cm yr<sup>-1</sup> for a surface area of 1 100 000 m<sup>2</sup> in 2021 (Table 2, Fig. 5a). Mean sedimentation rates progressively decrease through time with  $0.48 \pm 0.24$  cm yr<sup>-1</sup> for the period 2013-2021, and  $0.39 \pm 0.49$  cm yr<sup>-1</sup> for 2016-2021 (Table 2). LiDAR results also show an important spatial heterogeneity in marsh vertical evolution. Maximum vertical gains are found at the saltmarsh boundary and at the foot of the dikes, with values > +1.0 m for the period from 2010 to 2021. High sediment accumulation > +0.8 m also characterizes areas located close and along the channels (Fig 5a). In contrast, minimum gains below 0.1 m are found landward, and from the zones characterized by mowing activity in the northern bay.

LiDAR-based SAR estimates for the entire instrumental period are consistent with sediment-core data at the coring sites, except for the site cored in 2017 (Fig 5b). Data show an increasing trend along the cross-shore transect from shoreward to seaward coring locations. Reported LiDAR values for the coring locations of the northern transect AIG21\_22, 21, and 20 are 1.2, 2.2, and 2.9 cm yr<sup>-1</sup>, respectively for the period 2010-2021. LiDAR values for the coring locations of the eastern transect AIG21\_11, and AIG17\_01 are 2.2, and 3.2 cm yr<sup>-1</sup>, respectively. These values were derived using a 3 x 3 m grid around the coring sites to account for spatial variability and for the GPS uncertainty in locating the coring sites.

#### **4.4. Organic carbon accumulation rates**

Along the north transect, organic carbon accumulation rates (CAR) are marked by a great heterogeneity among the cores, reflecting varying rates of carbon deposition in different locations (Table 1). The landward location (AIG21\_22) displays the lowest CAR value of  $107 \pm 11 \text{ g cm}^{-2} \text{ yr}^{-1}$ , suggesting a relatively slower rate of organic carbon accumulation. In contrast, the intermediate location (AIG21\_21) and the seaward location (AIG21\_20) exhibit higher CAR values of  $373 \pm 5 \text{ g cm}^{-2} \text{ yr}^{-1}$  and  $340 \pm 29 \text{ g cm}^{-2} \text{ yr}^{-1}$ , respectively, indicating more rapid organic carbon deposition in these areas. The site closer to the river mouth (AIG21\_11) displayed an intermediate CAR value of  $182 \pm 48 \text{ g cm}^{-2} \text{ yr}^{-1}$  (Table 1). The heterogeneity in CAR values among the cores emphasizes the complexity of carbon dynamics in saltmarsh environments and highlights the need for site-specific investigations to understand the underlying processes governing sediment and carbon accumulation.

To estimate these CAR values, we used the organic carbon (OC) content measured by an elemental analyzer, ensuring that the results represented the true OC content in the sediment. We conducted multiple tests using different combustion durations and temperatures to verify the accuracy of the LOI (Loss on Ignition) technique for determining total organic carbon (TOC) percentages (Fig. S3). Our findings revealed that the LOI technique alone cannot be used for a quantitative determination of TOC percentages. As a result, we relied on the elemental analyzer to accurately assess the OC content and subsequently calculate the organic carbon accumulation rates.

## 5. Discussion

### 5.1. The Aiguillon Bay: a rapidly changing coastal environment

#### 5.1.1. Lateral and vertical evolution of the saltmarshes

Results have underlined a rapid progradation and aggradation of the saltmarshes in the Aiguillon Bay, at both multi-annual and multi-decadal scales.

The reconstructed evolution of the saltmarsh boundary revealed a lateral expansion of the marsh up to  $14 \text{ m yr}^{-1}$ , with a mean area gain of  $8 \text{ ha yr}^{-1}$  for the period 1950-2020 (Fig. 2). The saltmarsh boundary progressively recovered a general round shape, which contrasted with a more angular morphology induced by the most recent land claims in 1963 and 1965 (Fig. 3). At a smaller spatial scale, vegetated tips up to 300 m in length are clearly evidenced along the levees on both sides of the channels. These vegetated tips can act as barriers, providing a calmer environment conducive to sediment deposition, thus favoring the gradual expansion of the saltmarsh boundary (Fagherazzi et al., 2012; Verger, 2009). It is well established that halophytic vegetation canopy can reduce waves, currents and the associated bed shear stresses (Fagherazzi et al., 2020; Lavaud et al., 2020), which in turn can have profound impact on sedimentation patterns by increasing sediment trapping efficiency (Mudd et al., 2010; Temmerman et al., 2005).

Sediment core data revealed vertical accretion rates of  $0.8\text{-}2.2 \text{ cm yr}^{-1}$  (Fig. 4, 5; Table 1). Multi-decadal sediment accumulation rates (SAR) were estimated using  $^{210}\text{Pb}$ -based dating models developed for each sediment core (Fig. 4; Table 1). The log profiles of  $^{210}\text{Pb}$  activity showed a linear decrease through depth below the surface mixed layer, with consistent initial activity found among all cores (Arias-Ortiz et al., 2018). The  $^{137}\text{Cs}$  profiles were coherent with the  $^{210}\text{Pb}$  models for each core, with a clear  $^{137}\text{Cs}$  peak interpreted as the year 1963 found in AIG21\_22. It should be noted that an anomalous drop in  $^{210}\text{Pb}$  activity was found in the AIG21\_22 profile at c. 50 cm depth, and dated to  $1970 \pm 4 \text{ yrs}$ . Both a remobilization of older material and/or a higher sediment accumulation diluting the  $^{210}\text{Pb}$  signal could explain a decrease in  $^{210}\text{Pb}$  activity (Nolte et al., 2013). A possible explanation includes the remobilization of mudflat sediment by storm waves and its transport toward saltmarshes during marine flooding. Although no marine flooding event was reported for this period in the studied area (Breilh et al., 2014), a powerful storm occurred the 13 and 14 February of 1972. Wind gusts reached  $140 \text{ km h}^{-1}$  in La Rochelle, and a 89 cm-high storm surge was recorded at low tide in the mouth of the Loire Estuary, 130 km northwestward of the Aiguillon Bay (<https://www.bretagne.developpement-durable.gouv.fr/etude-vimers-des-evenements-de-tempete-en-bretagne-a2705.html>, <http://tempetes.meteo.fr>). Another possibility relates to the construction of embankments associated with the most recent land claim in 1965. Indeed, embankments are built of mud that is partly dug from the saltmarsh, which can lead to significant remobilization of old sediment material potentially redeposited in the vicinity of the coring site.

Multi-decadal sediment accumulation rates in the saltmarshes of the Aiguillon Bay ( $0.8\text{-}2.2 \text{ cm yr}^{-1}$ ) are among the highest reported for equivalent systems found in temperate regions (Giuliani and Bellucci, 2019; Fig. 6). In particular, SAR of the Aiguillon Bay exceed the global SAR value of  $2.4 \pm 0.5 \text{ mm yr}^{-1}$  reported for saltmarshes (Ouyang et al., 2022). LiDAR data for the period 2010-2021 tend to confirm the SAR orders of magnitude at the coring locations ( $1.2\text{-}2.9 \text{ cm yr}^{-1}$ ; Fig. 5b). Besides relatively high uncertainty in the vertical accuracy of the LiDAR DEM data, the consistency between the two techniques strengthens the reliability of SAR estimates from the cores. High sedimentation rates may appear surprising regarding the small size and the small water discharge of the rivers flowing in or close to the bay ( $2 \text{ m}^3 \text{ s}^{-1}$  for the Lay River, and  $12 \text{ m}^3 \text{ s}^{-1}$  for the Sèvre Niortaise River; Banque HYDRO, 1969/2017). Like in the Aiguillon Bay, very high sedimentation rates were also reported for the

Marennes-Oléron Bay, located 45 km to the south (Allard et al., 2010; Bertin et al., 2005; Bertin and Chaumillon, 2006; Poirier et al., 2016; Fig. 1). Four main sources of fine-grained sediment explain the rapid sediment-fill of the Marennes-Oléron Bay, including: (i) small coastal rivers flowing directly into the area; (ii) the Gironde estuary (to the south; Fig. 1); (iii) Mesozoic marls and limestones outcropping along the coast; and (iv) coastal marsh sediments. The Gironde estuary alone was found to account for up to 84 % of the sediment supplied to the Marennes-Oléron Bay (Dabrin et al., 2014). By analogy, it can be proposed that the sediment-fill of the Aiguillon Bay is not solely derived from the local rivers flowing close to or within the cove. The relative contribution of sediment supplied by the Gironde Estuary and by erosion of coastal marls and limestones remains unknown, but cannot be excluded.

Beyond the control by sediment supply, high sedimentation rates in the Aiguillon Bay can be related to both its morphology and history. The presence of a few kilometer-long sand spit in the West ("Pointe de l'Aiguillon"; Fig. 1) makes this bay a sheltered environment that prevents erosion and favors siltation (Verger, 2009). Also, the Aiguillon Bay inherited from a long history of land reclamation (Godet et al., 2015; Godet and Thomas, 2013; Fig. 1). This likely had led to a decrease in tidal prism favoring sediment deposition, itself inducing tidal prism decrease through a positive feedback mechanism (Ladd, 2021; Unger et al., 2016).

#### 5.1.2. Spatial heterogeneity in saltmarsh vertical evolution

Sedimentation rates obtained from the sediment core analysis showed an increasing trend along the two cross-shore transects, from shoreward to seaward locations (Fig 5). Also, SAR estimates did not differ significantly from the northern to the eastern transects, suggesting that the intra-site variability cannot be attributed to the proximity with the Sèvre Niortaise River. Instead, LiDAR mapping confirms the shoreward to seaward trend in SAR, with maxima found at the mudflat-saltmarsh transition, and on both sides of tidal channels and tidal creeks (Fig 5a).

Two main parameters can explain this spatial pattern: (i) the distance from the sediment source; and (ii) the duration of inundation, in turn related to the accommodation space between the marsh topography and the highest tide levels. Indeed, a longer and more frequent flooding of seaward areas of the saltmarsh may enhance sediment supply and deposition close to the sediment source provided by mudflats and tidal channels (Fagherazzi et al., 2020, 2012). In particular, the multi-year transects of the Aiguillon Bay illustrate the control of marsh evolution by accommodation space (Fig. 5b). The marsh topography seaward was under the mean high water springs (MHWS) in 2010. Six years later, this same zone was above MHWS showing the rapid sediment-fill of this accommodation space (Fig. 5b). Then, this topography stabilized between 2016 and 2021 revealing a weak sedimentation as accommodation space reduced considerably. The same applies at the scale of the entire bay. Sedimentation rates inferred from LiDAR were maximal for the period 2010-2021 ( $1.17 \pm 0.38 \text{ cm yr}^{-1}$ ) and progressively decreased towards the most recent period 2016-2021 ( $0.39 \pm 0.49 \text{ cm yr}^{-1}$ ; Table 2). It is well established that young and low-elevation saltmarshes rapidly expand up to an equilibrium elevation relative to highest water levels, while older and higher saltmarshes tend to maintain this equilibrium level (Temmerman et al., 2004; Unger et al., 2016). Zhang et al. (2019) also showed that sediment deposition on marsh platforms decreases exponentially with distance from the channels and from the marsh edge, as a function of decreasing water depth and sediment settling velocity landward.

It should also be noted that the most terrestrial zone of the northern saltmarsh is characterized by relatively lower elevations (i.e.,  $< 2.7 \text{ m NGF}$ ) located at a distance of 0 to 250 m from the embankment (northern transect; Fig. 5). This depression contrasts with the inner part of the eastern transect where the marsh topography gradually increases landward (Fig. 5b). Extensive and motorized mowing activity takes place in the northern bay (Godet et al., 2015; Joyeux et al., 2014), which is likely responsible for localized sediment compaction. This area also exhibits relatively high LiDAR-based SAR values (Fig. 5a).

They can be explained by both relatively large accommodation space, and by important sediment supply favored by the presence of gullies used to drain and clean out the mown zones.

### 5.1.3. The coastal marsh evolution offsets sea level rise impact

The combined approach based on sediment cores and LiDAR to estimate sedimentation rates sheds light on the response of saltmarshes to sea level rise over the last decades. It provides important clues on marsh resilience, with the mean accretion rates that largely outperform the local mean sea level rise of  $2.80 \pm 0.73 \text{ mm yr}^{-1}$  recorded in La Rochelle harbors (period 1993-2018, Fig. 1; Dodet et al., 2019; SONEL database, <http://www.sonel.org>). This suggests that the saltmarshes of the Aiguillon Bay are currently able to keep up with rising sea level. This has important implications with regards to services expected from such ecosystems, through adaptation to global sea level rise, protection from marine flood and shoreline erosion, and the support of ecosystem health and biodiversity (Bij de Vaate et al., 2020; Leonardi et al., 2018).

Interestingly, our data indicate positive accretion balance (accretion rate minus local sea-level rise rate) at both long and shorter term (Fig. 5b; Table 1, 2). This positive accretion balance in the Aiguillon Bay is consistent with what was observed in some other European sites (e.g., Silva et al., 2013), the Canadian Atlantic Coast and in the Gulf of Mexico (Crosby et al., 2016; Fig. 6). Sediment accumulation rates can vary greatly between marshes, which is explained by complex interactions between changes in relative sea level rise, tidal exchanges, vegetation type and density, and depositional processes (Giuliani and Bellucci, 2019). For instance, macrotidal marshes hold greater capacity to buffer rising sea level than microtidal ones, especially under high concentration of suspended sediment adjacent to the marsh (Friedrichs and Perry, 2022). Although it was not possible to detect storm events due to the relatively low resolution of the  $^{210}\text{Pb}$  profiles (with the exception of the hypothetical record of the 1972 storm), the history of intense and frequent storm events on the French Atlantic coast could have also favored marsh elevation (six events between 1924 and 2010; Breihl et al., 2014). During major marine flood events, tidal flats are eroded by storm waves and mud is transported and deposited shoreward onto saltmarshes and backshore environments (Baumann et al., 2017; Schuerch et al., 2018, 2013). The nature of inorganic sediment supplied to the saltmarshes during tides and storms are thus similar (e.g., grain size, TOC content). In this context, the wide mudflats of the Aiguillon Bay (3700 ha) provide a substantial source of erodible fine-grained material made available for supplying the saltmarshes during high tides and storm events.

## 5.2. Carbon accumulation rates in the saltmarshes

Organic carbon accumulation rates (CAR) calculated using the sediment cores of the Aiguillon Bay saltmarshes range from 107 to 373  $\text{g cm}^{-2} \text{ yr}^{-1}$ ; these values are consistent with the reviewed mean CAR value of  $245 \pm 26 \text{ g cm}^{-2} \text{ yr}^{-1}$  (Ouyang and Lee, 2014; Regnier et al., 2022; Fig. 6b). Given the rather low sediment OC content (1.3-6.0 %), it is very likely that these relatively high organic carbon accumulation rates are related to the fast sedimentation within saltmarshes of this bay. Similarly, Mueller et al., (2019) showed that long-term OC sequestration rates in minerogenic saltmarshes were primarily determined by sediment accumulation rates and to a far lesser degree by the variability in OC content. Results from the Aiguillon Bay will thus help refine blue carbon review efforts (Chmura et al., 2003; Duarte et al., 2005; Mcleod et al., 2011; Murray et al., 2011; Ouyang and Lee, 2014; Regnier et al., 2022), which till now, were fed by only one French study from Mediterranean estuarine saltmarshes (Hensel et al., 1999).

Our results also highlight an important spatial variability in OC accumulation capacity. This capacity is maximal for seaward and intermediate areas of the saltmarsh ( $340 \text{ g cm}^{-2} \text{ yr}^{-1}$  and  $373 \text{ g cm}^{-2} \text{ yr}^{-1}$ , respectively), minimal landward ( $107 \text{ g cm}^{-2} \text{ yr}^{-1}$ ), and in-between closer to the mouth of the Sèvre

Niortaise River ( $182 \text{ g cm}^{-2} \text{ yr}^{-1}$ ; Table 1). This variability questions the use of a unique CAR value in world review efforts, which should be best supported by multiple coring (e.g., Young et al., 2018). The heterogeneity in mass accumulation rates, used in the calculation of carbon accumulation rates, seem to be the main driver of the CAR spatial variability. This has important implications for estimating and upscaling OC accumulation rates for the studied region.

### 5.3. Particulate organic carbon source and stability

Van de Broek et al., (2018) stressed the fact that there might not be direct links between high OC deposition rates and high OC sequestration rates due to: (i) a potential source of allochthonous OC that is not sequestered in-situ, thus not contributing to the active removal of  $\text{CO}_2$  from the atmosphere; and (ii) OC decomposition at the surface of the marsh that can directly relates to the release of  $\text{CO}_2$  and  $\text{CH}_4$  gasses. Here, we discuss these two processes to account for to avoid overestimating saltmarsh OC sequestration rates (Leorri et al., 2018).

#### 5.3.1. Autochthonous vs. allochthonous organic carbon

Sediment organic carbon in saltmarshes have two sources: (i) autochthonous OC derived from roots, woody tissues and leaf litter (supplied by C3 and C4 marsh terrestrial vegetation); and (ii) allochthonous OC produced from external sources (land and marine) and trapped by the vegetation of the marsh (Krauss et al., 2018; Van de Broek et al., 2018). The main sources of sediment to the Aiguillon Bay have distinctly different  $\delta^{13}\text{C}$  and N/C compositions, which theoretically enables interpreting the origin of OC to the saltmarshes (Fig. 7).

$\delta^{13}\text{C}$  and N/C within surface and near-surface sediments show a terrestrial plant signature. The signature of surface samples from the landward site (AIG21\_22) tends toward a C3 vascular-plant signature, and towards a C4 plant signature for the seaward site (AIG21\_20) (Lamb et al., 2006; Fig. 7). Plant associations mapped by the National Natural Reserve support these results, with C3 plants such as Sea Purslane (*halimione portulacoides*) dominating landward areas of the salt marshes, and C4 plants like Marine Spartina (*spartina maritima*) developing preferentially seaward (Fig. S1). Previous studies similarly showed that C3 vascular vegetation can contribute largely to the organic carbon pool of supra-tidal sediments in minerogenic marshes (Wilson et al., 2005).

Contrasting with surface sediments, a marine source clearly dominates the OC signature of the deepest sediment samples (marine POC:  $\delta^{13}\text{C} = -25.1$  to  $-20.9 \text{ ‰}$ ; N/C = 0.13 to 0.24; SOMLIT station, Pertuis Antioche; Fig. 1a, Fig., 7). This marine signature strongly supports our interpretation that basal-core samples correspond to mudflat sediments ( $\delta^{13}\text{C} = -22.0 \pm 0.2 \text{ ‰}$ ; N/C =  $0.15 \pm 0.01$ ). Overlying these mudflat sediments, the saltmarsh sediment sections with stable OC are also placed within the range of the marine POC signature, but they differ significantly from the mudflat samples ( $\delta^{13}\text{C} = -23.5 \pm 0.4 \text{ ‰}$  for AIG21\_22,  $\delta^{13}\text{C} = -21.6 \pm 0.6 \text{ ‰}$  for AIG21\_20; N/C of  $0.13 \pm 0.01$ ; Fig. 7). First, this suggests that the sediment composition of stable-OC sections is controlled primarily by the supply of allochthonous OC of marine origin. Although primary production by plants can exceed allochthonous OC deposition in some minerogenic marshes, Tidally-derived particulate organic matter is for most cases the dominant source of organic material in minerogenic marshes (e.g., Lamb et al., 2006). Second, the different signature between mudflat and saltmarsh samples also suggests that a small part of in-situ produced biomass still accounts for the stable OC content of deep saltmarsh samples.

In an analogous study from minerogenic marshes in northern Belgium, Van de Broek et al., (2018) discriminated: (i) a short-term OC deposition composed of relatively labile OC originating from locally-produced biomass; and (ii) a long-term OC deposition controlled by the supply of stable allochthonous OC from a marine origin. These authors further demonstrated that autochthonous OC was the main component being mineralized upon burial. The same process likely explains the transitional signature



of Aiguillon sediments with depth: from a terrestrial plant signature towards a signature comparable to marine POC. Interestingly, our data suggests that this mechanism applies disregarding the surface plant composition (C3 or C4).

### 5.3.2. Sediment organic carbon stability

Sediment accumulation rates from the Aiguillon saltmarshes were estimated from the stable OC sections of each core corresponding to a systematic depth below c. 20 cm and overlying mudflat sediments. Although no data are available from pore water geochemistry (e.g., Koretsky et al., 2008; Yau et al., 2022), this section of the cores was considered as the effectively-preserved OC stock (Mueller et al., 2019; Fig. 3). Steep decline in OC content with sediment depth was associated with a significant  $\delta^{13}\text{C}$  change of c. 4 ‰; enriched with depth for C3-dominated sites, and depleted for C4-dominated sites (Fig. 8a). This change was interpreted as OC loss between topsoil layers and deeper levels of the cores through sustained decomposition, with  $\delta^{13}\text{C}$  enrichment or depletion that depends on plant species and tissue types (Kelleway et al., 2022).

To support this interpretation and assess the  $\delta^{13}\text{C}$  signature of the reactive carbon in Aiguillon sediments, we followed the approach developed by Komada et al., (2022). It is based on the assumption that total OC in a sample ( $C_s$ ) consists of two components: a reactive ( $C_r$ ) and a non-reactive ( $C_{nr}$ ), with each component having a fixed  $\delta^{13}\text{C}$  value  $\delta_r$  and  $\delta_{nr}$ , respectively. With  $\delta_s$  the  $\delta^{13}\text{C}$  value of total OC in the sample, the following formula can be defined:

$$C_s = C_r + C_{nr} \quad (1)$$

$$\delta_s C_s = \delta_r C_r + \delta_{nr} C_{nr} \quad (2)$$

Combining (1) and (2) to replace  $C_r$ , this gives the following:

$$\delta_s C_s = \delta_r C_s + C_{nr}(\delta_{nr} - \delta_r) \quad (3)$$

if  $\delta_{nr}$  and  $\delta_r$  are constant, then plotting  $\delta_s C_s$  against  $C_s$  of the samples should yield a straight line with slope equivalent to  $\delta_r$ . This approach applied to Aiguillon sediments indicates a  $\delta^{13}\text{C}$  signature of -28.1‰ and -12.2‰ for the reactive carbon ( $\delta_r$ ) related to surface C3 and C4 plants, respectively (Fig. 8b). Together with the averaged  $\delta^{13}\text{C}$  signature of mudflat samples of  $-22.0 \pm 0.2$  ‰, these results suggest that surface sediments from the Aiguillon Bay are composed predominantly of reactive OC (Fig. 8). Thus, it justifies discarding the upper c. 20 cm in the calculation of OC accumulation rates, at risk of largely overestimating the carbon sink capacity of Aiguillon saltmarshes.

Possible explanations for changes in OC and  $\delta^{13}\text{C}$  with depth include the preferential decomposition of autochthonous vs. allochthonous OC through highly oxidizing conditions near the surface (Mueller et al., 2019), preferential use of a labile OC pool by microbial decomposers and fungi (Menichetti et al., 2015), and  $\delta^{13}\text{C}$  fractionation between above- and below-ground biomass (Benner et al., 1987). This last process is unlikely regarding the consistent  $\delta^{13}\text{C}$  signature between C3 terrestrial plants (-21 to -32 ‰), C3 below-ground biomass in Aiguillon sediments ( $-27.0 \pm 0.8$  ‰), and the signature of reactive OC calculated for marsh sediments influenced by C3 vegetation (-27.9 ‰; Fig 7, 8a).

### 5.4. Implications for carbon sequestration

Overall, our results of  $\delta^{13}\text{C}$  and N/C from the Aiguillon Bay support previous findings that allochthonous carbon of marine origin prevails in long-term OC accumulation of minerogenic marshes (e.g., Mueller et al., 2019; Van de Broek et al., 2018). Although the surface OC pool is for the most part of autochthonous origin, only a small fraction remains preserved with sediment depth, thus contributing to long-term carbon sequestration in the Aiguillon saltmarshes, which rate average  $2.5 \text{ Mg C ha}^{-1} \text{ yr}^{-1}$ .

634 Although the implications for C-crediting approaches has yet to be clarified (e.g., Mueller et al., 2019),  
635 the ability of coastal ecosystems to trap and store large amounts of allochthonous carbon from  
636 adjacent ecosystems remains a major asset with respect to the carbon sink function (e.g., Jennerjahn,  
637 2020). Our results imply that the wealth of the long-term carbon sequestration rates in minerogenic  
638 coastal marshes does not only depend on the marsh morphological evolution and the OC burial  
639 capacity of the vegetation. It also depends on the quality of coastal ecosystems at a larger scale, which  
640 includes nearshore waters and mudflat primary productivity. This calls on the need for more  
641 integrative coastal science, in which saltmarshes are considered as part of a coupled mudflat-marsh  
642 system, for instance (Schuerch et al., 2019). This coupling was emphasized among the top-ten pending  
643 questions to help prioritize the future of blue carbon science (Macreadie et al., 2019).

## 6. Conclusions

The saltmarshes of the Aiguillon Bay have shown great ability to cope with sea level rise, by elevating their topography at rates among the highest reported worldwide for these depositional environments. Our results highlighted the key role of sedimentation in providing and in maintaining ecosystem services offered by coastal wetlands. At present, the Aiguillon Bay still holds relatively important accommodation space, which enables it to expand both laterally and vertically at significant rates. The study site has inherited a long history of considerable sediment-fill of the Marais Poitevin, and it is still today characterized by significant sediment accumulation rates and volume gains. This suggests encouraging conditions for the resilience of the saltmarshes of the Aiguillon Bay in the face of future climate change and sea level rise. Nevertheless, as the source of sediment is not known precisely and in what quantity, it remains difficult to predict the future evolution of saltmarshes in the bay.

Our findings support previous research showing that marine-derived carbon dominates long-term organic carbon accumulation in minerogenic coastal marshes, while only a small fraction of locally-produced carbon is preserved deeper in the sediment. This suggests that carbon accumulation rates in these saltmarshes depend not only on marsh morphology and vegetation's carbon burial capacity but also on the broader coastal ecosystem, including nearshore waters and mudflat productivity. Integrative coastal science, viewing saltmarshes as part of a coupled mudflat-marsh system, appears essential to better understand carbon dynamics and sequestration rates in these coastal wetlands.

Increasing the value and recognition of the key role of intertidal ecosystems were also suggested as a potential lever to help sustain high biological production in coastal ecosystems. In particular, raising public awareness through communication of scientific knowledge can play an important role for integrating adaptation and mitigation options (IPCC, 2022). Among the multiple supports, popularization of science intended for the general public have shown to be particularly efficient in this regard (Chaumillon et al., 2019, 2021; <https://pnr.parc-marais-poitevin.fr/la-mer-contre-attaque-le-nouveau-show-scientifique-debarque-a-la-rochelle-mardi-26-novembre-2019>). Another way to increase the value of intertidal ecosystems is through the prism of natural heritage. The transdisciplinary consortia in which this study is framed by (ANR Project PAMPAS: '*Evolution of the Heritage Identity of the Pertuis Charentais marshes in response to the hazard of marine submersion*'), may enable to open such perspectives.

## 673 **Acknowledgment**

674 This work was financed by two transdisciplinary consortia that are the ANR project PAMPAS (# ANR-  
675 18-CE32-0006-01) and La Rochelle Territoire Zero Carbone (LRTZC, Carbon Bleu Axe2 # OPE-2021-0376,  
676 # OPE-2021-0496), and supported by the LIFE project “Baie de l’Aiguillon”, LIFE14 NAT/FR/000669  
677 (January 1<sup>th</sup> 2016 -June 30 2022). We would like to thank the team of the ‘Réserve Naturelle Nationale  
678 de la Baie de l’Aiguillon’. Special thanks go to Paméla Lagrange (LPO), Régis Gallais (OFB), Jean-Pierre  
679 Guéret (LPO), and Frédéric Robin (LPO) for their support with fieldwork, for sharing their expertise,  
680 and for data access. We are also grateful to Laurent Godet (LETG, Nantes University) for sharing  
681 georeferenced data about the historical land claims and evolution of the saltmarsh boundary in the  
682 Aiguillon Bay. Particular thanks go to Christophe Petit (ArScAn, University Paris 1) and Vincent Bichet  
683 (ChronoEnvironnement, UBFC) for their support with fieldwork material, and to Aurélie Pace, and  
684 Jasson Mora Mussio (LIENSs, CNRS-La Rochelle University) for their help with the coring field  
685 campaigns. We would like also to thank Guillou Gaël and Benoit Lebreton (LIENSs, CNRS-La Rochelle  
686 University) for their support with the IRMS platform. Special thanks go to Christine Dupuy for her  
687 support and Anaïs Schmitt (LIENSs, CNRS-La Rochelle University) for active discussion about the  
688 sediment dynamics of the Gironde estuary and Pertuis sea Marine Nature Park (CELHYSE Project).

## 689 References

- 690 Allard, J., Chaumillon, E., Bertin, X., Poirier, C., Ganthy, F., 2010. Sedimentary record of  
 691 environmental changes and human interferences in a macrotidal bay for the last millenaries:  
 692 the Marennes-Oléron Bay (SW France). *Bull. Société Géologique Fr.* 181, 151–169.  
 693 <https://doi.org/10.2113/gssgfbull.181.2.151>
- 694 Arias-Ortiz, A., Masqué, P., Garcia-Orellana, J., Serrano, O., Mazarrasa, I., Marbà, N., Lovelock, C.E.,  
 695 Lavery, P.S., Duarte, C.M., 2018. Reviews and syntheses:  $\delta^{13}\text{C}$ -  
 696 derived sediment and carbon accumulation rates in vegetated coastal ecosystems – setting  
 697 the record straight. *Biogeosciences* 15, 6791–6818. [https://doi.org/10.5194/bg-15-6791-](https://doi.org/10.5194/bg-15-6791-2018)  
 698 2018
- 699 Baumann, J., Chaumillon, E., Schneider, J.-L., Jorissen, F., Sauriau, P.-G., Richard, P., Bonnin, J.,  
 700 Schmidt, S., 2017. Contrasting sediment records of marine submersion events related to  
 701 wave exposure, Southwest France. *Sediment. Geol.* 353, 158–170.  
 702 <https://doi.org/10.1016/j.sedgeo.2017.03.009>
- 703 Baustian, M.M., Stagg, C.L., Perry, C.L., Moss, L.C., Carruthers, T.J.B., Allison, M., 2017. Relationships  
 704 Between Salinity and Short-Term Soil Carbon Accumulation Rates from Marsh Types Across a  
 705 Landscape in the Mississippi River Delta. *Wetlands* 37, 313–324.  
 706 <https://doi.org/10.1007/s13157-016-0871-3>
- 707 Benner, R., Fogel, M.L., Sprague, E.K., Hodson, R.E., 1987. Depletion of  $^{13}\text{C}$  in lignin and its  
 708 implications for stable carbon isotope studies. *Nature* 329, 708–710.  
 709 <https://doi.org/10.1038/329708a0>
- 710 Bertin, X., Bruneau, N., Breilh, J.-F., Fortunato, A.B., Karpytchev, M., 2012. Importance of wave age  
 711 and resonance in storm surges: The case Xynthia, Bay of Biscay. *Ocean Model.* 42, 16–30.  
 712 <https://doi.org/10.1016/j.ocemod.2011.11.001>
- 713 Bertin, X., Chaumillon, E., 2006. The implication of oyster farming in increasing sedimentation rates in  
 714 a macrotidal bay: the Marennes-Oléron Bay, France 5.
- 715 Bertin, X., Chaumillon, E., Sottolichio, A., Pedreros, R., 2005. Tidal inlet response to sediment infilling  
 716 of the associated bay and possible implications of human activities: the Marennes-Oléron  
 717 Bay and the Maumusson Inlet, France. *Cont. Shelf Res.* 25, 1115–1131.  
 718 <https://doi.org/10.1016/j.csr.2004.12.004>
- 719 Bertin, X., Li, K., Roland, A., Zhang, Y.J., Breilh, J.F., Chaumillon, E., 2014. A modeling-based analysis of  
 720 the flooding associated with Xynthia, central Bay of Biscay. *Coast. Eng.* 94, 80–89.  
 721 <https://doi.org/10.1016/j.coastaleng.2014.08.013>
- 722 Bertram, C., Quaas, M., Reusch, T.B.H., Vafeidis, A.T., Wolff, C., Rickels, W., 2021. The blue carbon  
 723 wealth of nations. *Nat. Clim. Change* 11, 704–709. [https://doi.org/10.1038/s41558-021-](https://doi.org/10.1038/s41558-021-01089-4)  
 724 01089-4
- 725 Bij de Vaate, I., Brückner, M.Z.M., Kleinhans, M.G., Schwarz, C., 2020. On the Impact of Salt Marsh  
 726 Pioneer Species-Assemblages on the Emergence of Intertidal Channel Networks. *Water*  
 727 *Resour. Res.* 56. <https://doi.org/10.1029/2019WR025942>
- 728 Breilh, J.-F., Bertin, X., Chaumillon, E., Giloy, N., Sauzeau, T., 2014. How frequent is storm-induced  
 729 flooding in the central part of the Bay of Biscay? *Glob. Planet. Change* 122, 161–175.  
 730 <https://doi.org/10.1016/j.gloplacha.2014.08.013>
- 731 Breilh, J.F., Chaumillon, E., Bertin, X., Gravelle, M., 2013. Assessment of static flood modeling  
 732 techniques: application to contrasting marshes flooded during Xynthia (western France). *Nat.*  
 733 *Hazards Earth Syst. Sci.* 13, 1595–1612. <https://doi.org/10.5194/nhess-13-1595-2013>
- 734 Chaumillon, E., Proust, J.-N., Menier, D., Weber, N., 2008. Incised-valley morphologies and  
 735 sedimentary-fills within the inner shelf of the Bay of Biscay (France): A synthesis. *J. Mar. Syst.*  
 736 72, 383–396. <https://doi.org/10.1016/j.jmarsys.2007.05.014>
- 737 Chaumillon, E., Tessier, B., Weber, N., Tesson, M., Bertin, X., 2004. Buried sandbodies within present-  
 738 day estuaries (Atlantic coast of France) revealed by very high resolution seismic surveys. *Mar.*  
 739 *Geol.* 211, 189–214.

- Chmura, G.L., Anisfeld, S.C., Cahoon, D.R., Lynch, J.C., 2003. Global carbon sequestration in tidal, saline wetland soils. *Glob. Biogeochem. Cycles* 17, n/a-n/a. <https://doi.org/10.1029/2002GB001917>
- Coignot, E., Polsenaere, P., Soletchnik, P., et al., 2020. Variabilité spatio-temporelle des nutriments et du carbone et flux associés le long d'un continuum terrestres-aquatique tempéré (Marais Poitevin – Baie de l'Aiguillon – Pertuis Breton). Rapport final (suivi 2017-2018), IFREMER. Archived in : ARCHIMER Ifremer's institutional repository.
- Collin, A., Long, B., Archambault, P., 2010. Salt-marsh characterization, zonation assessment and mapping through a dual-wavelength LiDAR. *Remote Sens. Environ.* 114, 520–530. <https://doi.org/10.1016/j.rse.2009.10.011>
- Constantin, S., Doxaran, D., Derkacheva, A., Novoa, S., Lavigne, H., 2018. Multi-temporal dynamics of suspended particulate matter in a macrotidal river Plume (the Gironde) as observed by satellite data. *Estuar. Coast. Shelf Sci.* 202, 172–184. <https://doi.org/10.1016/j.ecss.2018.01.004>
- Corbett, D.R., Walsh, J.P., 2015. <sup>210</sup>Pb and <sup>137</sup>Cs: establishing a chronology for the last century, in: Shennan, I., Long, A.J., Horton, B.P. (Eds.), *Handbook of Sea-Level Research*. John Wiley & Sons, Ltd, Chichester, UK, pp. 361–372. <https://doi.org/10.1002/9781118452547.ch24>
- Costanza, R., de Groot, R., Sutton, P., van der Ploeg, S., Anderson, S.J., Kubiszewski, I., Farber, S., Turner, R.K., 2014. Changes in the global value of ecosystem services. *Glob. Environ. Change* 26, 152–158. <https://doi.org/10.1016/j.gloenvcha.2014.04.002>
- Craft, C.B., Seneca, E.D., Broome, S.W., 1991. Loss on Ignition and Kjeldahl Digestion for Estimating Organic Carbon and Total Nitrogen in Estuarine Marsh Soils: Calibration with Dry Combustion. *Estuaries* 14, 175. <https://doi.org/10.2307/1351691>
- Crosby, S.C., Sax, D.F., Palmer, M.E., Booth, H.S., Deegan, L.A., Bertness, M.D., Leslie, H.M., 2016. Salt marsh persistence is threatened by predicted sea-level rise. *Estuar. Coast. Shelf Sci.* 181, 93–99. <https://doi.org/10.1016/j.ecss.2016.08.018>
- Dabrin, A., Schäfer, J., Bertrand, O., Masson, M., Blanc, G., 2014. Origin of suspended matter and sediment inferred from the residual metal fraction: Application to the Marennes Oleron Bay, France. *Cont. Shelf Res.* 72, 119–130. <https://doi.org/10.1016/j.csr.2013.07.008>
- DataLab France, 2022. Chiffres clés du climat: France, Europe et Monde. Ministère de la Transition écologique, France. <https://www.statistiques.developpement-durable.gouv.fr/edition-numerique/chiffres-cles-du-climat-2022/avant-propos>.
- Dodet, G., Bertin, X., Bouchette, F., Gravelle, M., Testut, L., Wöppelmann, G., 2019. Characterization of Sea-level Variations Along the Metropolitan Coasts of France: Waves, Tides, Storm Surges and Long-term Changes. *J. Coast. Res.* 88, 10. <https://doi.org/10.2112/SI88-003.1>
- Doxaran, D., Froidefond, J.-M., Castaing, P., Babin, M., 2009. Dynamics of the turbidity maximum zone in a macrotidal estuary (the Gironde, France): Observations from field and MODIS satellite data. *Estuar. Coast. Shelf Sci.* 81, 321–332. <https://doi.org/10.1016/j.ecss.2008.11.013>
- Duarte, C.M., Middelburg, J.J., Caraco, N., 2005. Major role of marine vegetation on the oceanic carbon cycle 8.
- Dubosq, N., Schmidt, S., Walsh, J.P., Grémare, A., Gillet, H., Lebleu, P., Poirier, D., Perello, M.-C., Lamarque, B., Deflandre, B., 2021. A first assessment of organic carbon burial in the West Gironde Mud Patch (Bay of Biscay). *Cont. Shelf Res.* 221, 104419. <https://doi.org/10.1016/j.csr.2021.104419>
- Dupuy C., Agogué H., Amann B., Azémar F., Becu N., et al., 2022. Towards carbon neutrality by 2040 in La Rochelle metropolitan area (France): quantifying the role of wetlands and littoral zone in the capture and sequestration of blue carbon. ECSA 59: Using the best scientific knowledge for the sustainable management of estuaries and coastal seas will take place in San Sebastian, Spain from 5-8 September 2022. hal-03777579
- Fagherazzi, S., Kirwan, M.L., Mudd, S.M., Guntenspergen, G.R., Temmerman, S., D'Alpaos, A., van de Koppel, J., Rybczyk, J.M., Reyes, E., Craft, C., Clough, J., 2012. Numerical models of salt marsh

evolution: Ecological, geomorphic, and climatic factors. *Rev. Geophys.* 50, RG1002.  
<https://doi.org/10.1029/2011RG000359>

Fagherazzi, S., Mariotti, G., Leonardi, N., Canestrelli, A., Nardin, W., Kearney, W.S., 2020. Salt Marsh Dynamics in a Period of Accelerated Sea Level Rise. *J. Geophys. Res. Earth Surf.* 125.  
<https://doi.org/10.1029/2019JF005200>

Ford, M., 2012. Shoreline Changes on an Urban Atoll in the Central Pacific Ocean: Majuro Atoll, Marshall Islands. *J. Coast. Res.* 279, 11–22. <https://doi.org/10.2112/JCOASTRES-D-11-00008.1>

Friedrichs, C.T., Perry, J.E., 2022. Tidal Salt Marsh Morphodynamics: A Synthesis 32.

Giuliani, S., Bellucci, L.G., 2019. Salt Marshes: Their Role in Our Society and Threats Posed to Their Existence, in: *World Seas: An Environmental Evaluation*. Elsevier, pp. 79–101.  
<https://doi.org/10.1016/B978-0-12-805052-1.00004-8>

Godet, L., Pourinet, L., Joyeux, E., Verger, F., 2015. Dynamique spatiale et usage des schorres de l’Anse de l’Aiguillon de 1705 à nos jours. *Enjeux de conservation d’un patrimoine naturel littoral marin*. Cybergeog. <https://doi.org/10.4000/cybergeog.26774>

Godet, L., Thomas, A., 2013. Three centuries of land cover changes in the largest French Atlantic wetland provide new insights for wetland conservation. *Appl. Geogr.* 42, 133–139.  
<https://doi.org/10.1016/j.apgeog.2013.05.011>

Hendriks, K., Gubbay, S., Arets, E., Janssen, J., 2020. Carbon storage in European ecosystems: a quick scan for terrestrial and marine EUNIS habitat types. Wageningen, Wageningen Environmental Research, Internal Report. 66 pp. 87.

Hensel, P.F., Day Jr., J.W., Pont, D., 1999. Wetland Vertical Accretion and Soil Elevation Change in the Rhone River Delta, France: The Importance of Riverine Flooding. *J. Coastal Res.* 15, 668–681.

Himes-Cornell, A., Pendleton, L., Atiyah, P., 2018. Valuing ecosystem services from blue forests: A systematic review of the valuation of salt marshes, sea grass beds and mangrove forests. *Ecosyst. Serv.* 30, 36–48. <https://doi.org/10.1016/j.ecoser.2018.01.006>

Himmelstoss, E.A., Henderson, R.E., Kratzmann, M.G., Farris, A.S., 2018. Digital Shoreline Analysis System DSAS Version 5.0 User Guide.” Open-File Report 2018-1179: 126. Open-File Report 1179, 126.

Howard, J., Hoyt, S., Insensee, K., Telszewski, M., Pidgeon, E., 2014. Coastal Blue Carbon: Methods for assessing carbon stocks and emissions factors in mangroves, tidal salt marshes, and seagrasses. Conservation International, Intergovernmental Oceanographic Commission of UNESCO, International Union for Conservation of Nature, Arlington, Virginia, USA.

IPCC, 2022. Climate Change 2022: Mitigation of Climate Change. Skea et al., Working Group III contribution to the Sixth Assessment Report of the Intergovernmental Panel on Climate Change. Summary for Policymakers 99.

Iurian, A.R., Millward, G., Blake, W., Abril Hernández, J.M., 2021. Fine-tuning of 210Pb-based methods for dating vegetated saltmarsh sediments. *Quat. Geochronol.* 62, 101153.  
<https://doi.org/10.1016/j.quageo.2021.101153>

Jennerjahn, T.C., 2020. Relevance and magnitude of “Blue Carbon” storage in mangrove sediments: Carbon accumulation rates vs. stocks, sources vs. sinks. *Estuar. Coast. Shelf Sci.* 247, 107027.  
<https://doi.org/10.1016/j.ecss.2020.107027>

Joyeux, E., Blanchet, R., Haie, S., Carpentier, A., 2014. La gestion des prés salés de la baie de l’Aiguillon: vers une approche fonctionnelle. In: *Faune sauvage*, 302. 38–43.

Kelleway, J.J., Trevathan-Tackett, S.M., Baldock, J., Critchley, L.P., 2022. Plant litter composition and stable isotope signatures vary during decomposition in blue carbon ecosystems. *Biogeochemistry* 158, 147–165. <https://doi.org/10.1007/s10533-022-00890-3>

Komada, T., Bravo, A., Brinkmann, M., Lu, K., Wong, L., Shields, G., 2022. “Slow” and “fast” in blue carbon: Differential turnover of allochthonous and autochthonous organic matter in minerogenic salt marsh sediments. *Limnol. Oceanogr.* Ino.12090.  
<https://doi.org/10.1002/Ino.12090>

- Koretsky, C.M., Haveman, M., Cuellar, A., Beuving, L., Shattuck, T., Wagner, M., 2008. Influence of Spartina and Juncus on Saltmarsh Sediments. I. Pore Water Geochemistry. *Chem. Geol.* 255, 87–99. <https://doi.org/10.1016/j.chemgeo.2008.06.013>
- Krauss, K.W., Noe, G.B., Duberstein, J.A., Conner, W.H., Stagg, C.L., Cormier, N., Jones, M.C., Bernhardt, C.E., Graeme Lockaby, B., From, A.S., Doyle, T.W., Day, R.H., Ensign, S.H., Pierfelice, K.N., Hupp, C.R., Chow, A.T., Whitbeck, J.L., 2018. The Role of the Upper Tidal Estuary in Wetland Blue Carbon Storage and Flux. *Glob. Biogeochem. Cycles* 32, 817–839. <https://doi.org/10.1029/2018GB005897>
- Ladd, C.J.T., 2021. Review on processes and management of saltmarshes across Great Britain. *Proc. Geol. Assoc.* 15.
- Lamb, A.L., Wilson, G.P., Leng, M.J., 2006. A review of coastal palaeoclimate and relative sea-level reconstructions using  $\delta^{13}\text{C}$  and C/N ratios in organic material. *Earth-Sci. Rev.* 75, 29–57. <https://doi.org/10.1016/j.earscirev.2005.10.003>
- Lavaud, L., Lechevalier, A., Coulombier, T., Bertin, X., Martins, K., 2020. Effet de la végétation sur la dissipation des vagues au niveau d'un pré salé. XVIèmes Journées Nationales Génie Côtier – Génie Civil. Le Havre, 2020. <https://doi.org/10.5150/jngcgc.2020.010>
- Leonardi, N., Carnacina, I., Donatelli, C., Ganju, N.K., Plater, A.J., Schuerch, M., Temmerman, S., 2018. Dynamic interactions between coastal storms and salt marshes: A review. *Geomorphology* 301, 92–107. <https://doi.org/10.1016/j.geomorph.2017.11.001>
- Leorri, E., Zimmerman, A.R., Mitra, S., Christian, R.R., Fatela, F., Mallinson, D.J., 2018. Refractory organic matter in coastal salt marshes-effect on C sequestration calculations. *Sci. Total Environ.* 633, 391–398. <https://doi.org/10.1016/j.scitotenv.2018.03.120>
- Lovelock, C.E., Reef, R., 2020. Variable Impacts of Climate Change on Blue Carbon. *One Earth* 3, 195–211. <https://doi.org/10.1016/j.oneear.2020.07.010>
- Macreadie, P.I., Anton, A., Raven, J.A., Beaumont, N., Connolly, R.M., Friess, D.A., Kelleway, J.J., Kennedy, H., Kuwae, T., Lavery, P.S., Lovelock, C.E., Smale, D.A., Apostolaki, E.T., Atwood, T.B., Baldock, J., Bianchi, T.S., Chmura, G.L., Eyre, B.D., Fourqurean, J.W., Hall-Spencer, J.M., Huxham, M., Hendriks, I.E., Krause-Jensen, D., Laffoley, D., Luisetti, T., Marbà, N., Masque, P., McGlathery, K.J., Megonigal, J.P., Murdiyarso, D., Russell, B.D., Santos, R., Serrano, O., Silliman, B.R., Watanabe, K., Duarte, C.M., 2019. The future of Blue Carbon science. *Nat. Commun.* 10, 3998. <https://doi.org/10.1038/s41467-019-11693-w>
- Mcleod, E., Chmura, G.L., Bouillon, S., Salm, R., Björk, M., Duarte, C.M., Lovelock, C.E., Schlesinger, W.H., Silliman, B.R., 2011. A blueprint for blue carbon: toward an improved understanding of the role of vegetated coastal habitats in sequestering  $\text{CO}_2$ . *Front. Ecol. Environ.* 9, 552–560. <https://doi.org/10.1890/110004>
- Medeiros, S.C., Bobinsky, J.S., Abdelwahab, K., 2022. Locality of topographic ground truth data for salt marsh lidar DEM elevation bias mitigation. *IEEE J. Sel. Top. Appl. Earth Obs. Remote Sens.* 1–10. <https://doi.org/10.1109/JSTARS.2022.3189226>
- Menichetti, L., Houot, S., van Oort, F., Kätterer, T., Christensen, B.T., Chenu, C., Barré, P., Vasilyeva, N.A., Ekblad, A., 2015. Increase in soil stable carbon isotope ratio relates to loss of organic carbon: results from five long-term bare fallow experiments. *Oecologia* 177, 811–821. <https://doi.org/10.1007/s00442-014-3114-4>
- Mudd, S.M., D'Alpaos, A., Morris, J.T., 2010. How does vegetation affect sedimentation on tidal marshes? Investigating particle capture and hydrodynamic controls on biologically mediated sedimentation. *J. Geophys. Res.* 115, F03029. <https://doi.org/10.1029/2009JF001566>
- Mueller, P., Ladiges, N., Jack, A., Schmiedl, G., Kutzbach, L., Jensen, K., Nolte, S., 2019. Assessing the long-term carbon-sequestration potential of the semi-natural salt marshes in the European Wadden Sea. *Ecosphere* 10. <https://doi.org/10.1002/ecs2.2556>
- Murray, B.C., Pendleton, L., Jenkins, W.A., Sifleet, S., 2011. Green Payments for Blue Carbon. Economic Incentives for Protecting Threatened Coastal Habitats Nicholas Institute for Environmental Policy Solutions Report NI R 11-04, 52.



- Nolte, S., Koppelaar, E.C., Esselink, P., Dijkema, K.S., Schuerch, M., De Groot, A.V., Bakker, J.P., Temmerman, S., 2013. Measuring sedimentation in tidal marshes: a review on methods and their applicability in biogeomorphological studies. *J. Coast. Conserv.* 17, 301–325. <https://doi.org/10.1007/s11852-013-0238-3>
- Ouyang, X., Connolly, R.M., Lee, S.Y., 2022. Revised global estimates of resilience to sea level rise for tidal marshes. *Environ. Chall.* 9, 100593. <https://doi.org/10.1016/j.envc.2022.100593>
- Ouyang, X., Lee, S.Y., 2020. Improved estimates on global carbon stock and carbon pools in tidal wetlands. *Nat. Commun.* 11, 317. <https://doi.org/10.1038/s41467-019-14120-2>
- Ouyang, X., Lee, S.Y., 2014. Updated estimates of carbon accumulation rates in coastal marsh sediments. *Biogeosciences* 11, 5057–5071. <https://doi.org/10.5194/bg-11-5057-2014>
- Poirier, C., Poitevin, C., Chaumillon, É., 2016. Comparison of estuarine sediment record with modelled rates of sediment supply from a western European catchment since 1500. *Comptes Rendus Geosci.* 348, 479–488. <https://doi.org/10.1016/j.crte.2015.02.009>
- Regnier, P., Resplandy, L., Najjar, R.G., Ciais, P., 2022. The land-to-ocean loops of the global carbon cycle. *Nature* 603, 401–410. <https://doi.org/10.1038/s41586-021-04339-9>
- Reyss, J.-L., Schmidt, S., Legeleux, F., Bonté, P., 1995. Large, low background well-type detectors for measurements of environmental radioactivity. *Nucl. Instrum. Methods Phys. Res.* 357, 391–397. [https://doi.org/10.1016/0168-9002\(95\)00021-6](https://doi.org/10.1016/0168-9002(95)00021-6)
- Rogers, K., Kelleway, J.J., Saintilan, N., Megonigal, J.P., Adams, J.B., Holmquist, J.R., Lu, M., Schile-Beers, L., Zawadzki, A., Mazumder, D., Woodroffe, C.D., 2019. Wetland carbon storage controlled by millennial-scale variation in relative sea-level rise. *Nature* 567, 91–95. <https://doi.org/10.1038/s41586-019-0951-7>
- Schuerch, M., Spencer, T., Evans, B., 2019. Coupling between tidal mudflats and salt marshes affects marsh morphology. *Mar. Geol.* 412, 95–106. <https://doi.org/10.1016/j.margeo.2019.03.008>
- Schuerch, M., Spencer, T., Temmerman, S., Kirwan, M.L., Wolff, C., Lincke, D., McOwen, C.J., Pickering, M.D., Reef, R., Vafeidis, A.T., Hinkel, J., Nicholls, R.J., Brown, S., 2018. Future response of global coastal wetlands to sea-level rise. *Nature* 561, 231–234. <https://doi.org/10.1038/s41586-018-0476-5>
- Schuerch, M., Vafeidis, A., Slawig, T., Temmerman, S., 2013. Modeling the influence of changing storm patterns on the ability of a salt marsh to keep pace with sea level rise: SALT MARSH ACCRETION AND STORM ACTIVITY. *J. Geophys. Res. Earth Surf.* 118, 84–96. <https://doi.org/10.1029/2012JF002471>
- Schmitt A., Chaumillon E., 2023. Understanding morphological evolution and sediment dynamics at multi-time scales helps balance human activities and protect coastal ecosystems: an example with the Gironde and Pertuis Marine Park. *Sci. Tot. Env.* 887, 163819
- Silva, T.A., Freitas, M.C., Andrade, C., Taborda, R., Freire, P., Schmidt, S., Antunes, C., 2013. Geomorphological response of the salt-marshes in the Tagus estuary to sea level rise. *J. Coast. Res.* 65, 582–587. <https://doi.org/10.2112/SI65-099.1>
- Stupar, Y.V., Schäfer, J., García, M.G., Schmidt, S., Piovano, E., Blanc, G., Huneau, F., Le Coustumer, P., 2014. Historical mercury trends recorded in sediments from the Laguna del Plata, Córdoba, Argentina. *Geochemistry* 74, 353–363. <https://doi.org/10.1016/j.chemer.2013.11.002>
- Temmerman, S., Bouma, T.J., Govers, G., wang, Z.B., De Vries, M. B., Herman, P.M.J., 2005. Impact of vegetation on flow routing and sedimentation patterns: Three-dimensional modeling for a tidal marsh. *J Geophys Res* 110. <https://doi.org/10.1029/2005JF000301>
- Temmerman, S., Govers, G., Wartel, S., Meire, P., 2004. Modelling estuarine variations in tidal marsh sedimentation: response to changing sea level and suspended sediment concentrations. *Mar. Geol.* 212, 1–19. <https://doi.org/10.1016/j.margeo.2004.10.021>
- Unger, V., Elsey-Quirk, T., Sommerfield, C., Velinsky, D., 2016. Stability of organic carbon accumulating in *Spartina alterniflora*-dominated salt marshes of the Mid-Atlantic U.S. *Estuar. Coast. Shelf Sci.* 182, 179–189. <https://doi.org/10.1016/j.ecss.2016.10.001>
- Van de Broek, M., Vandendriessche, C., Poppelmonde, D., Merckx, R., Temmerman, S., Govers, G., 2018. Long-term organic carbon sequestration in tidal marsh sediments is dominated by old-

aged allochthonous inputs in a macrotidal estuary. *Glob. Change Biol.* 24, 2498–2512.  
<https://doi.org/10.1111/gcb.14089>

Verger, F., 2009. *Zones humides du littoral français*, Belin. ed. Paris.

Vinent, O.D., Johnston, R.J., Kirwan, M.L., Leroux, A.D., Martin, V.L., 2019. Coastal dynamics and adaptation to uncertain sea level rise: Optimal portfolios for salt marsh migration. *J. Environ. Econ. Manag.* 98, 102262. <https://doi.org/10.1016/j.jeem.2019.102262>

Wilson, C.A., Allison, M.A., 2008. An equilibrium profile model for retreating marsh shorelines in southeast Louisiana. *Estuar. Coast. Shelf Sci.* 80, 483–494.  
<https://doi.org/10.1016/j.ecss.2008.09.004>

Wilson, G.P., Lamb, A.L., Leng, M.J., Gonzalez, S., Huddart, D., 2005. Variability of organic  $\delta^{13}\text{C}$  and C/N in the Mersey Estuary, U.K. and its implications for sea-level reconstruction studies. *Estuar. Coast. Shelf Sci.* 64, 685–698. <https://doi.org/10.1016/j.ecss.2005.04.003>

Windham-Myers, L., Crooks, S., Troxler, T.G., 2019. *A Blue Carbon Primer: The State of Coastal Wetland carbon Science, Practice, and Policy*. Taylor & Francis Group, LLC, Boca Raton, FL 33487-2742.

Yau, Y.Y.Y., Xin, P., Chen, X., Zhan, L., Call, M., Conrad, S.R., Sanders, C.J., Li, L., Du, J., Santos, I.R., 2022. Alkalinity export to the ocean is a major carbon sequestration mechanism in a macrotidal saltmarsh 13.

Young, M.A., Macreadie, P.I., Duncan, C., Carnell, P.E., Nicholson, E., Serrano, O., Duarte, C.M., Shiell, G., Baldock, J., Ierodiaconou, D., 2018. Optimal soil carbon sampling designs to achieve cost-effectiveness: a case study in blue carbon ecosystems. *Biol. Lett.* 14, 20180416.  
<https://doi.org/10.1098/rsbl.2018.0416>

Zhang, X., Leonardi, N., Donatelli, C., Fagherazzi, S., 2019. Fate of cohesive sediments in a marsh-dominated estuary. *Adv. Water Resour.* 125, 32–40.  
<https://doi.org/10.1016/j.advwatres.2019.01.003>

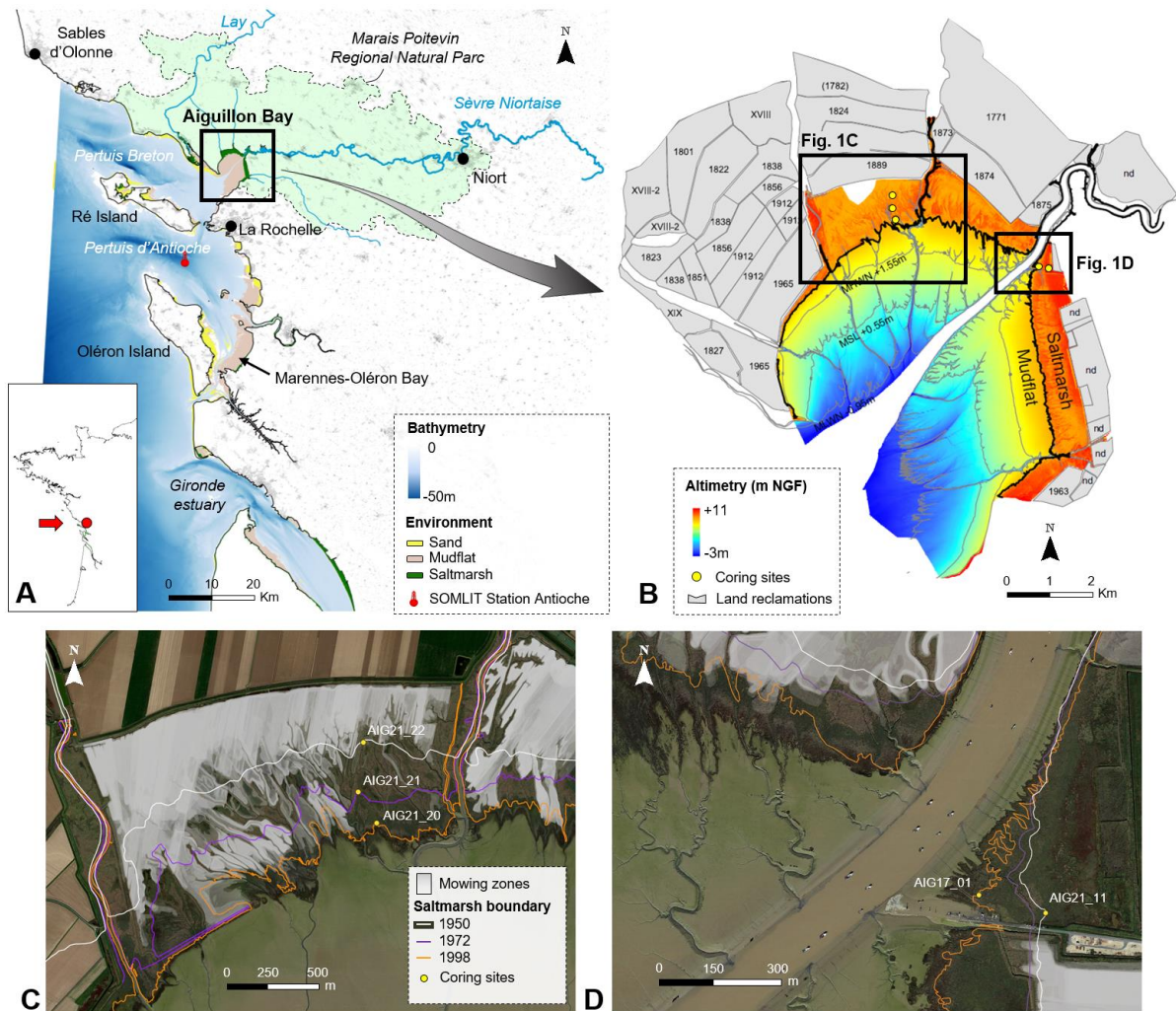


**Figure 1** **A** Location of the study site on the French Atlantic Coast, integrated in the Marais Poitevin Regional Natural Park. The coastal bathymetry was downloaded from the SHOM (<https://diffusion.shom.fr/>). **B** Topography of the Aiguillon Bay in 2021, placed in the history of land reclamation mapped by Godet et al., (2015). **C** and **D** Satellite images showing the location of the coring sites along cross-shore transects in the bay North and East, respectively. The coring sites were chosen outside the mowing areas (gradual gray zones), and on a historical saltmarsh boundary.

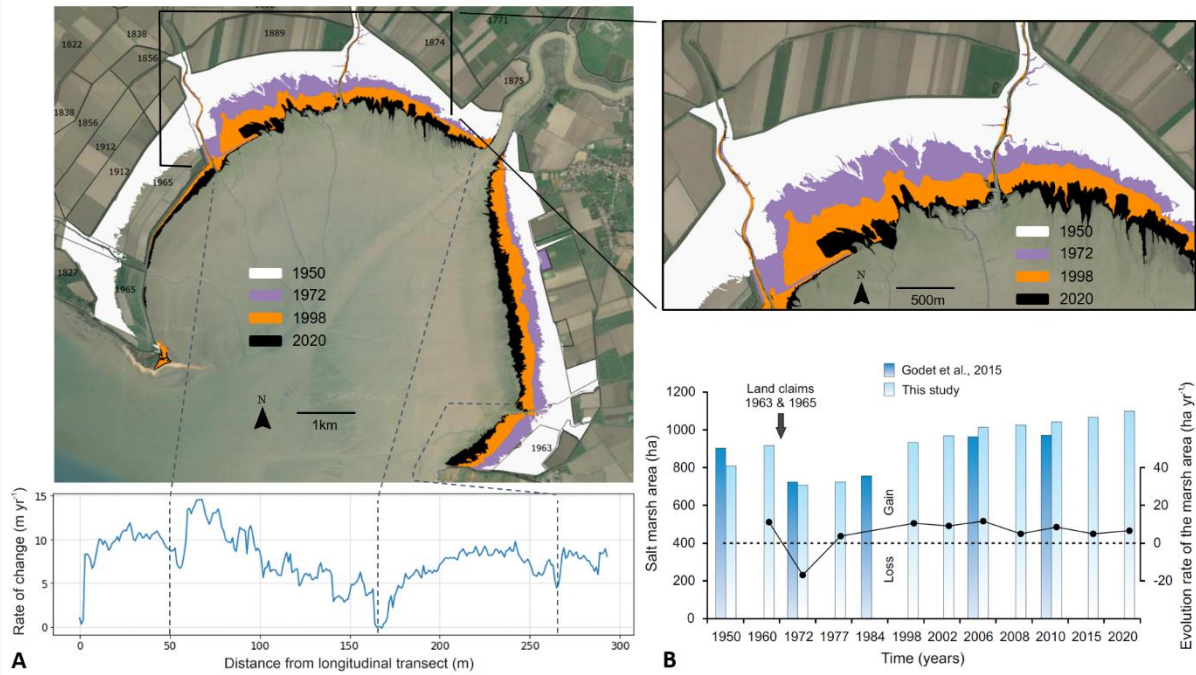


**Figure 2** Evolution of the saltmarsh boundary and area since 1950. **A** (*upper*) spatial progradation of the saltmarsh area, and (*lower left*) progradation rates (in m yr<sup>-1</sup>) calculated along a longitudinal transect for the period 1950-2020. **B** Temporal evolution of the saltmarsh area (in ha) and rates of change (in ha yr<sup>-1</sup>), for the whole bay. The vertical arrow marks the most recent land claims in 1963 and 1965, which induced an important reduction in the saltmarsh area. Data are from this study and Godet et al. (2015).

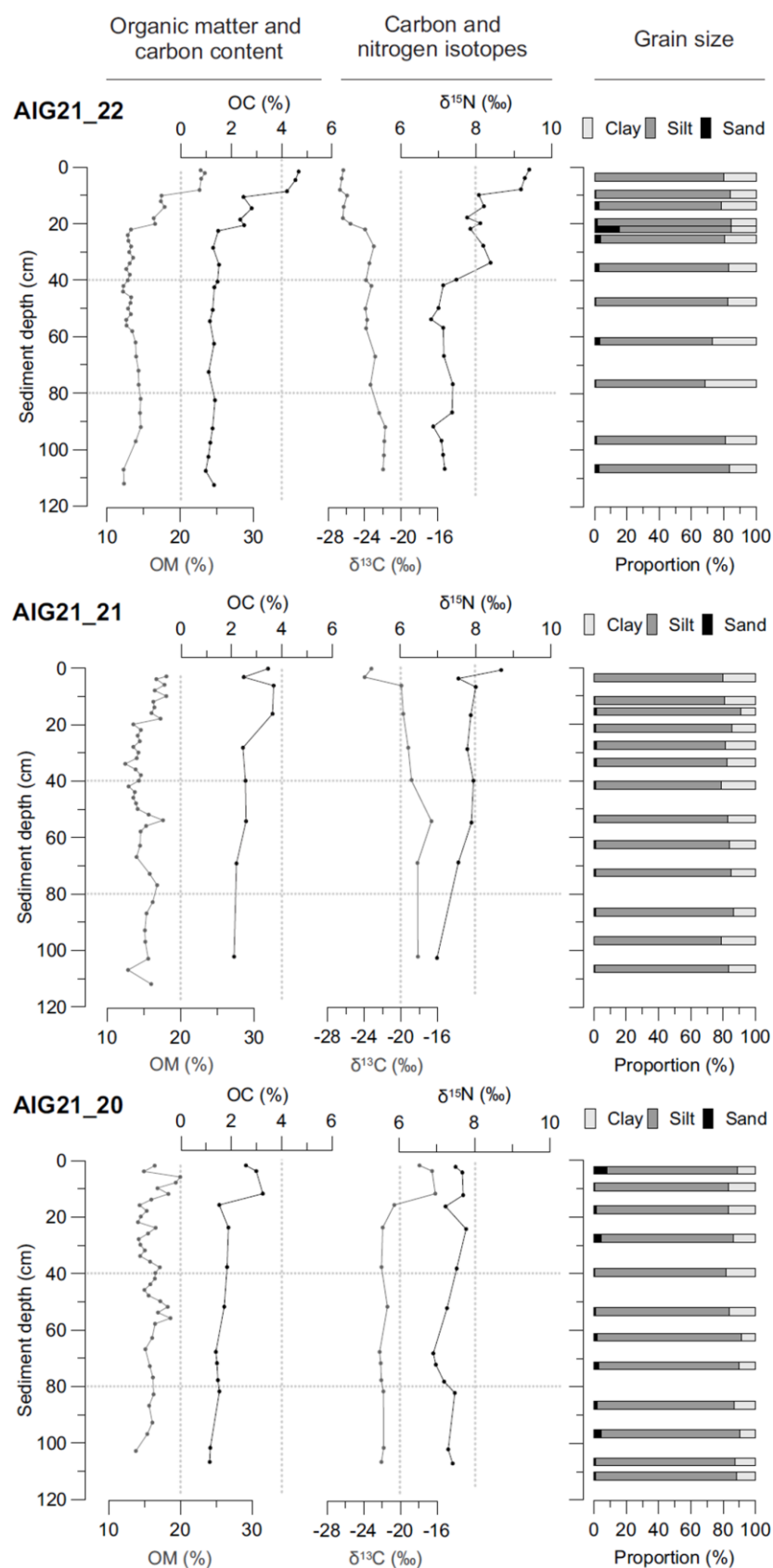
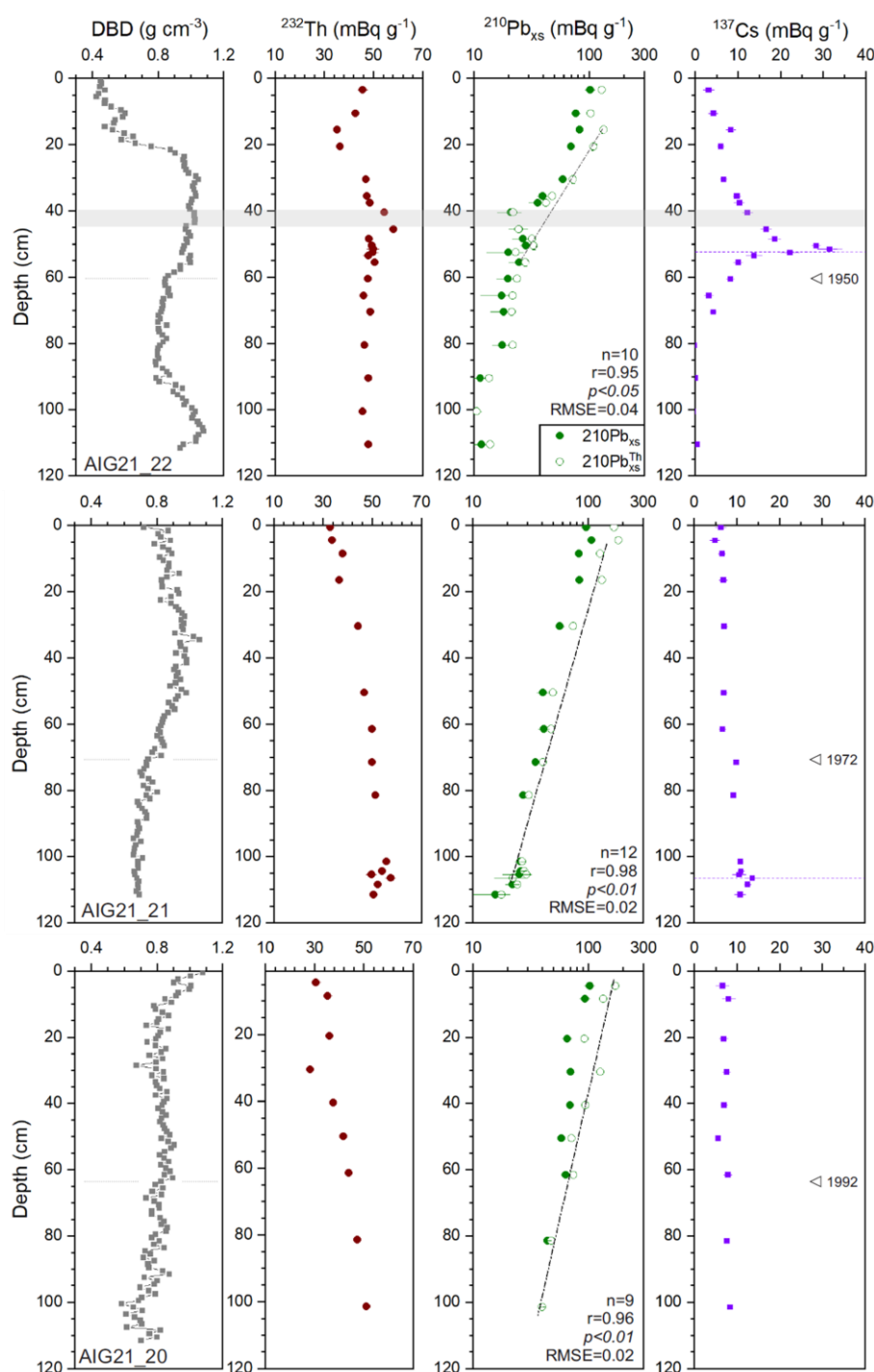


**Figure 3** Downcore profiles of OM and OC content, carbon and nitrogen isotopes, and grain size fractions of the three cores of the northern transect. The grain-size distribution of each sediment samples (*light gray*) and the average per core (*black*) are also presented.



992

993 **Figure 4** Profiles with sediment depth of dry bulk density (DBD; gray),  $^{232}\text{Th}$  (red),  $^{210}\text{Pb}_{\text{xs}}$  and  $^{210}\text{Pb}_{\text{xs}}^{\text{Th}}$   
 994 (filled and empty green circles, respectively), and  $^{137}\text{Cs}$  (purple) for the three cores of the northern  
 995 transect. The exponential regressions from the  $^{210}\text{Pb}_{\text{xs}}^{\text{Th}}$  profiles are used to calculate sediment and  
 996 mass accumulation rates. The gray horizontal rectangular in the AIG21\_22 profile highlights an  
 997 anomaly in  $^{210}\text{Pb}_{\text{xs}}$ . The corresponding layer thickness was subtracted to produce an event-free  $^{210}\text{Pb}_{\text{xs}}^{\text{Th}}$   
 998 profile from which sediment accumulation rate was calculated. The dates on the y-axis correspond to  
 999 the saltmarsh boundary (reconstructed using aerial photographs and satellite images) on which the  
 1000 sediment core was retrieved. It marks the transition with depth between a tidal flat and a saltmarsh  
 1001 environment.



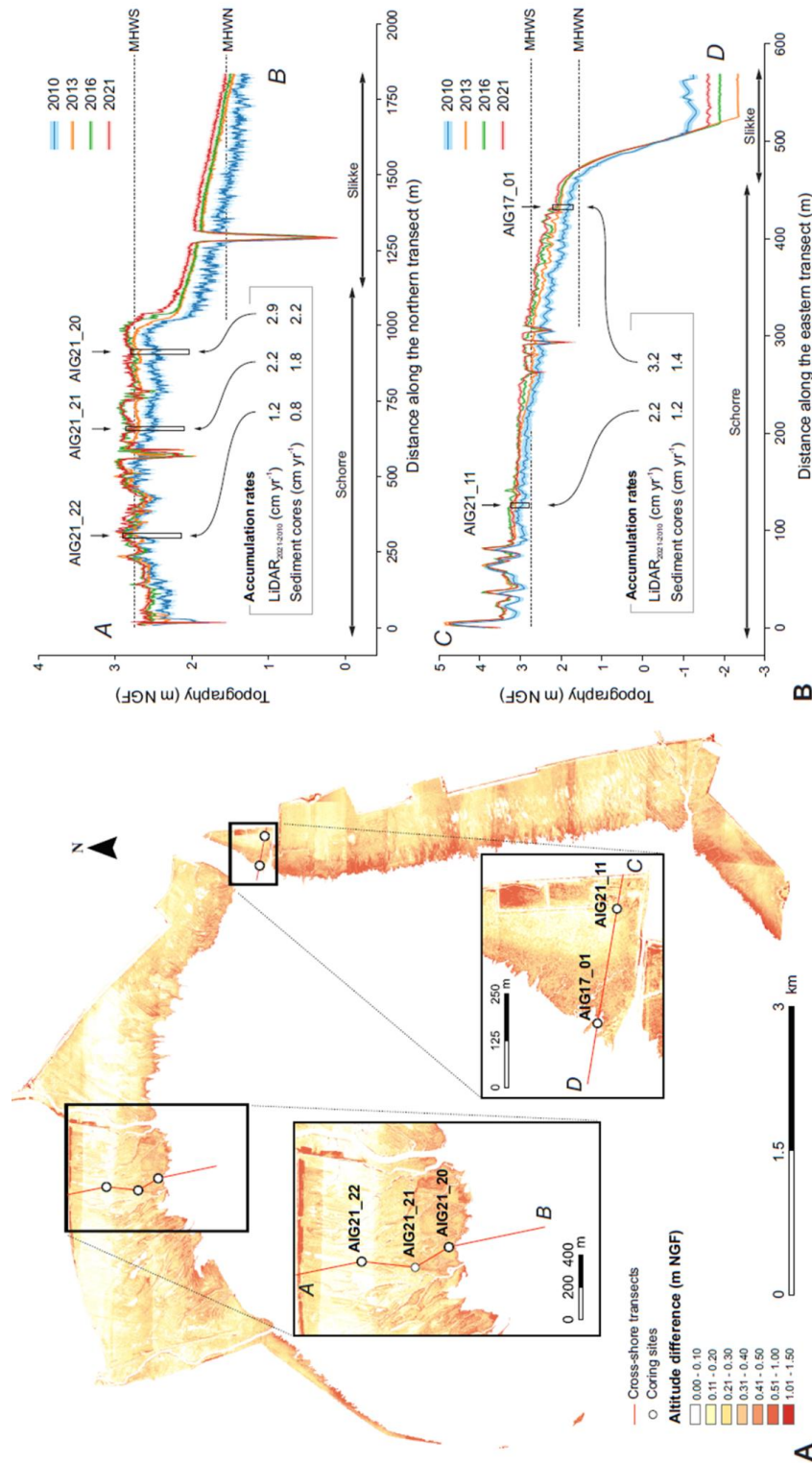
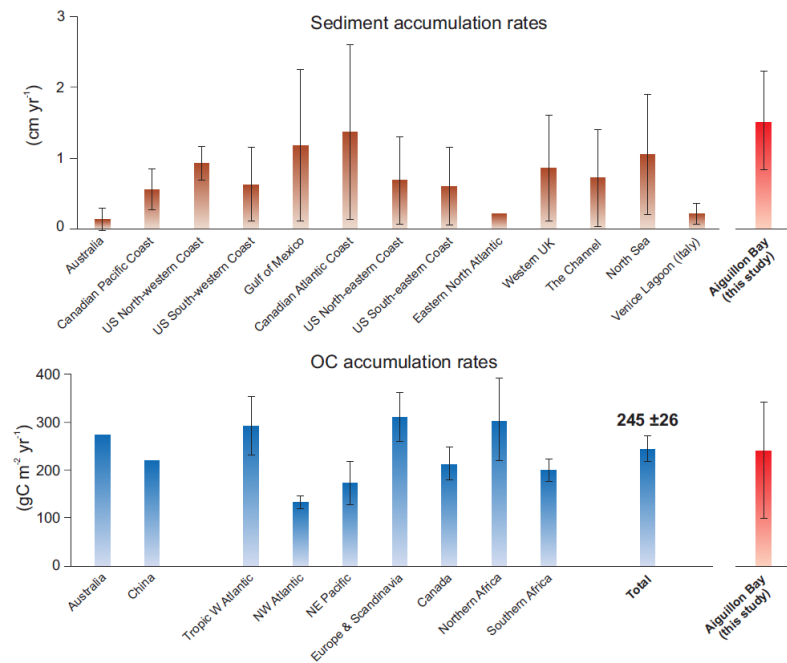


**Figure 5** Mapping of the vertical evolution of the saltmarsh in the Aiguillon Bay using LiDAR data. **A** DEMs difference between 2021 and 2010 with the location of the coring transects. **B** Topographical changes along the two cross-shore transects for the four different years of LiDAR acquisition. Lower-elevation peaks in the profiles mark the presence of channels and/or creeks crossed by the transects. The coring sites are also reported on the topographical evolution of the transects, thus allowing a direct comparison with <sup>210</sup>Pb-based accumulation rates [note that LiDAR accumulation rates (cm yr<sup>-1</sup>) are calculated for the period 2010-2021; Table 2]. MHWS, and MHWN dashed lines represent the level of mean high water springs and mean high water neaps, respectively.



1011

1012 **Figure 6** Comparison between the Aiguillon Bay (red bars) and other saltmarsh studies: for sediment  
 1013 accumulation rates from temperate regions (*upper panel*), and OC accumulation rates from other  
 1014 regions worldwide (*lower panel*). This figure was built using review data from Giuliani and Bellucci  
 1015 (2019) for sediment accumulation rates, and from Ouyang and Lee (2014) for OC accumulation rates.



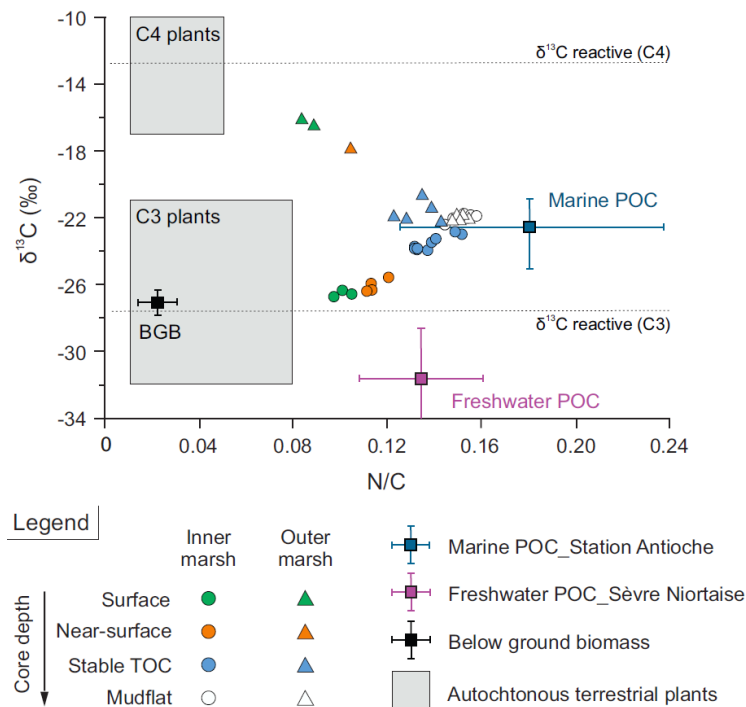
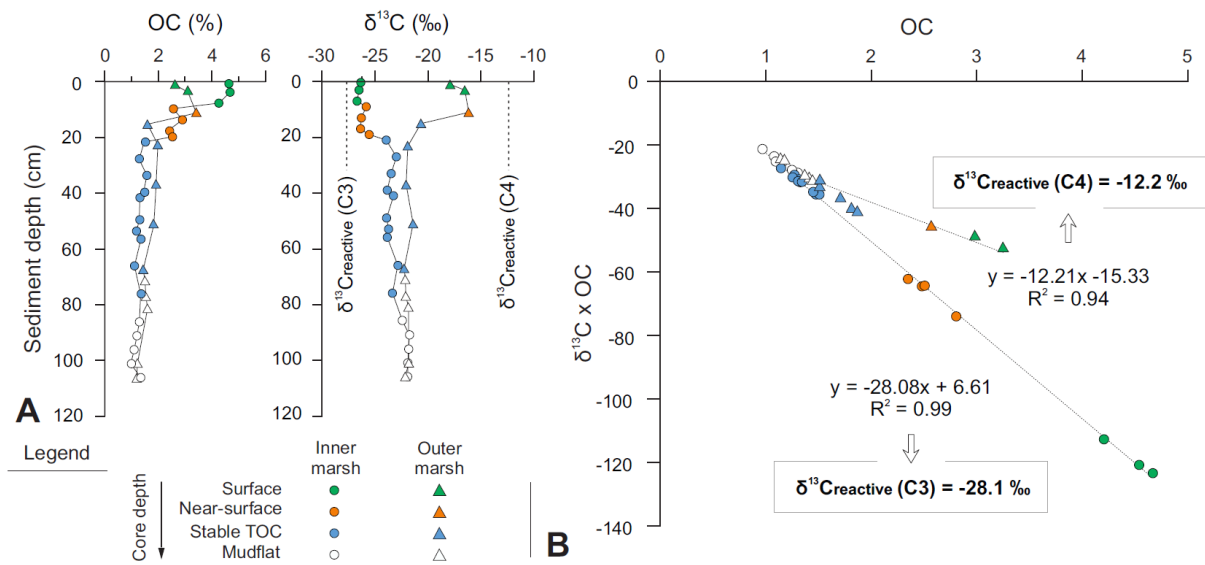


**Figure 7** Comparison of  $\delta^{13}\text{C}$  and N/C signatures of the Aiguillon saltmarsh sediments to OM sources. The use of the N/C ratio instead of C/N allows better separating the OM sources, graphically. Sediments are classified according to the position of the core on the saltmarsh: inner (*circles*) and outer (*triangles*), and to the depth in the core. The potential OM sources considered are: (i) freshwater POC from upstream the Sèvre Niortaise, in Marans (*purple square with error bars*; Richard, 2000); (ii) marine POC in the Pertuis d'Antioche (*blue square with error bars*; SOMLIT data); and (iii) C3- and C4-based autochthonous OM from saltmarsh (Lamb et al., 2006 and references therein). The signature of below-ground biomass from the inner marsh is also reported (BGB, *black square with error bars*; this study). Horizontal dashed lines refer to the isotopic signature of reactive sedimentary OC dominated by C3 and C4 plants (*cf. Fig. 8b*).

1027



1028

1029  
1030  
1031  
1032  
1033  
1034  
1035

**Figure 8** Elementary and isotopic signatures of saltmarsh sediments for the landward site (*circles*) and the seaward site (*triangles*), colored according to sediment depth. **A** Depth-profiles of OC and  $\delta^{13}\text{C}$ . Mudflat and marsh samples characterized by stable OC differ significantly from surface and near-surface samples by their OC content and  $\delta^{13}\text{C}$  signature. **B**  $\delta^{13}\text{C} \times \text{OC}$  against OC used to determine the signature of reactive OC as proposed by Komada et al. (2022). The slopes derived from cores of the inner and outer marsh suggest a  $\delta^{13}\text{C}_{\text{reactive}}$  of -12.2 ‰ and -28.1 ‰ for sediments influenced by C4 and C3 vegetation, respectively.

**Table 1** Data compilation by site for the saltmarshes of the Aiguillon Bay, with sediment accumulation rates (SAR in cm yr<sup>-1</sup>), mass accumulation rates (MAR, in g m<sup>-2</sup> yr<sup>-1</sup>), OC content (in %), and OC accumulation rates (CAR, in g m<sup>-2</sup> yr<sup>-1</sup>). The error bound to sedimentation rates refers to the propagation of the error on the slope the <sup>210</sup>Pb exponential regressions. \* Cores were too short to observe the <sup>137</sup>Cs peak; \*\* SAR and MAR are based on <sup>210</sup>Pb<sub>xs</sub>, without Th standardizing.

Site	Core coordinates		<sup>137</sup> Cs peak position		SAR		MAR		OC	
			depth	cumulative-mass	based on <sup>137</sup> Cs	based on <sup>210</sup> Pb <sub>xs</sub> Th	based on <sup>137</sup> Cs	based on <sup>210</sup> Pb <sub>xs</sub> Th	content	CAR
	Latitude	Longitude	(cm)	(g cm <sup>-2</sup> )	(cm yr <sup>-1</sup> )	(cm yr <sup>-1</sup> )	(g cm <sup>-2</sup> yr <sup>-1</sup> )	(g cm <sup>-2</sup> yr <sup>-1</sup> )	(%)	(gC m <sup>-2</sup> yr <sup>-1</sup> )
Northern transect										
<b>AIG21_20</b>	46.31111	-1.17439	> 112 *	> 90.5*	> 1.91*	<b>2.22 ± 0.32</b>	> 1.55*	1.83 ± 0.30	1.86 ± 0.16	<b>340 ± 29</b>
<b>AIG21_21</b>	46.31292	-1.17615	106.5	88.3	1.82	<b>1.85 ± 0.09</b>	1.51	1.50 ± 0.07	2.49 ± 0.03	<b>373 ± 5</b>
<b>AIG21_22</b>	46.31591	-1.17592	51	41.8	0.87	<b>0.84 ± 0.06</b>	0.71	0.74 ± 0.05	1.44 ± 0.15	<b>107 ± 11</b>
Eastern transect										
<b>AIG17_01</b>	46.303183	-1.13131				<b>1.41 ± 0.19</b>		1.24 ± 0.20 **		
<b>AIG21_11</b>	46.30252	-1.12912	> 36 *	> 25.2 *	> 0.61 *	<b>1.24 ± 0.26</b>	> 0.43*	0.86 ± 0.12	2.12 ± 0.56	<b>182 ± 48</b>

**Table 2** Evolution through time of the sediment volume gain (in m<sup>3</sup>) and sediment accumulation rates (in cm y<sup>-1</sup>) in saltmarshes of the whole bay inferred using LiDAR data. Values are calculated for the entire instrumental period (2010 to 2021) and more recent periods (2013 to 2021, and 2016 to 2021).

	2010 – 2021	2013 – 2021	2016 – 2021
	(entire instrumental period)		
Sediment volume gain (m <sup>3</sup> )	1 419 043 ± 458 732	426 251 ± 213 116	216 426 ± 267 440
Salt marsh area in 2021 (m <sup>2</sup> )	11 000 200 ± 1 200	11 000 200 ± 1 200	11 000 000 ± 1 200
Sediment accumulation rate (cm yr <sup>-1</sup> )	1.17 ± 0.38	0.48 ± 0.24	0.39 ± 0.49